Saumya Sengupta
Subhananda Chakrabarti

Structural, Optical and Spectral Behaviour of InAs-based Quantum Dot Heterostructures

Applications for High-performance Infrared Photodetectors

Springer

Structural, Optical and Spectral Behaviour of InAs-based Quantum Dot Heterostructures

Saumya Sengupta · Subhananda Chakrabarti

Structural, Optical and Spectral Behaviour of InAs-based Quantum Dot Heterostructures

Applications for High-performance Infrared Photodetectors

Springer

Saumya Sengupta
Department of Electrical Engineering
Indian Institute of Technology Bombay
Mumbai, Maharashtra
India

Subhananda Chakrabarti
Department of Electrical Engineering
Indian Institute of Technology Bombay
Mumbai, Maharashtra
India

ISBN 978-981-10-5701-4 ISBN 978-981-10-5702-1 (eBook)
DOI 10.1007/978-981-10-5702-1

Library of Congress Control Number: 2017946056

© Springer Nature Singapore Pte Ltd. 2018
This work is subject to copyright. All rights are reserved by the Publisher, whether the whole or part of the material is concerned, specifically the rights of translation, reprinting, reuse of illustrations, recitation, broadcasting, reproduction on microfilms or in any other physical way, and transmission or information storage and retrieval, electronic adaptation, computer software, or by similar or dissimilar methodology now known or hereafter developed.
The use of general descriptive names, registered names, trademarks, service marks, etc. in this publication does not imply, even in the absence of a specific statement, that such names are exempt from the relevant protective laws and regulations and therefore free for general use.
The publisher, the authors and the editors are safe to assume that the advice and information in this book are believed to be true and accurate at the date of publication. Neither the publisher nor the authors or the editors give a warranty, express or implied, with respect to the material contained herein or for any errors or omissions that may have been made. The publisher remains neutral with regard to jurisdictional claims in published maps and institutional affiliations.

Printed on acid-free paper

This Springer imprint is published by Springer Nature
The registered company is Springer Nature Singapore Pte Ltd.
The registered company address is: 152 Beach Road, #21-01/04 Gateway East, Singapore 189721, Singapore

Preface

This monograph is based on research into the structural, optical and spectral properties of InAs/(In)(Al)GaAs quantum dot (QD) heterostructures, grown by using molecular beam epitaxy (MBE) with an ultimate aim to fabricate high-performance quantum dot infrared photodetectors (QDIPs).

Since the introduction of intersubband photodetectors, much attention has focused on III–V semiconductor-based, MBE-grown quantum dot (QD) heterostructures for medium- and long-wavelength infrared-imaging technology. The three-dimensional carrier confinement possible with QDs is predicted to provide better performance than available from its quantum well counterpart. We optimized various MBE growth parameters using single-layer InAs/GaAs QDs and investigated their structural, optical and spectral properties. Then, we explored the effects of growth pause or ripening time on the properties of dots. The introduction of growth pause during the growth can extend the emission wavelength of the QDs. We have also examined the effects of post-growth rapid thermal annealing (RTA) treatment on properties of single-layer QDs. The next part of the work studied InAs/GaAs bilayer QD heterostructures with very thin ($\sim$7.5–8.5 nm) spacer layers. We have optimized minimum spacer thickness required to grow electronically coupled bilayer QD heterostructures. We have also established the superiority of bilayer QD heterostructures over the single-layer and uncoupled multilayer QD heterostructure in terms of optical and structural properties. We have examined the effects of RTA on bilayer QDs and found remarkable thermal stability of the same at high annealing temperature. Finally, we used sub-monolayer (SML) growth technique to grow QDs. This recent technique is expected to improve the electronics properties of the dots compared to those grown with the conventional Stranski–Krastanov (S-K) growth mode. After an initial study on material characterization, we established that SML QDIPs can be considered as a potential alternative to the conventional S-K QDIPs based on the comparison of the device performance.

Mumbai, India

Saumya Sengupta
Subhananda Chakrabarti

Acknowledgements

We would like to express our gratitude to Prof. Sanjay Krishna for providing Saumya the opportunity to work under him at University of New Mexico.

We would like to thank all the members of Prof. Krishna's group for their support and help.

We would also like to thank Dr. Nilanjan Halder, Dr. Ajit Barve and Dr. J.O. Kim for their guidance and help.

We would like to thank our group-members Dr. Arjun Mandal, Dr. Saurabh Nagar, Dr. Sourav Adhikary, Kulasekaran M., Hemant Ghadi, Goma K.C., Aijaz Ahmad, Saikalash Shetty, Akshay Balgarkashi, Jay Agawane, K.L. Mathur for their assistance and cooperation.

We would like to thank Shreyas Shah, Srujan Meesala and Akshay Agarwal for helping us in various stage of our research work.

We would like to thank Sandeep, Pradeep, Arvind, Arun, Sunil, Rajesh, Rajendra, Bhimraj and other staff members of Nanofabrication Laboratory, IIT Bombay for their help during our research work. The SPM Facility at IIT Bombay is also acknowledged for carrying out the AFM measurements of our samples.

We would also like to thank all the staff members working at the microelectronics and electrical office for all their administrative support and help.

Saumya would like to thank all the professors who have taught him at IIT Bombay. He is greatly indebted to them for sharing their wealth of knowledge with him.

We would like to acknowledge Science and Engineering Research Board-Department of Science and Technology (SERB-DST) and Indian Space and Research Organization (ISRO) for their financial support to carry out our work. We would also like to thank the Nanofabrication laboratory, IIT Bombay, for providing the world-class facility for research.

Contents

1 Introduction to Infrared Detectors and Quantum Dots 1
1.1 Introduction and Evolution of IR Detectors 2
1.2 Introduction to Quantum Dots 4
1.3 Motivation and Objective of the Work 8
1.4 Conclusion 10
References 10

2 Structural, Optical and Spectral Characterization of Single-Layer QDIPs 13
2.1 Introduction 13
2.2 Results and Discussion 14
2.2.1 Structural Characterization 14
2.2.2 Optical Characterization 17
2.2.3 Spectral Characterization of Device 20
2.3 Conclusions 21
References 22

3 Structural and Optical Characterization of Bilayer QD Heterostructures 25
3.1 Introduction 26
3.2 Results and Discussions 27
3.2.1 Structural Characterization 27
3.2.2 Optical Characterization 29
3.3 Comparison of Single-Layer, Bilayer and Multilayer QD Heterostructures 36
3.3.1 Introduction 36
3.3.2 Structural Characterization 36
3.3.3 Optical Characterization 37
3.4 Conclusions 40
References 41

4 Optical and Spectral Characterization of Sub-monolayer QDIPs . . . 43
4.1 Introduction . . . 43
4.2 Optimization of the SML Heterostructure . . . 45
4.2.1 Results and Discussions . . . 46
4.3 Demonstration of High-Performance SML QDIPs . . . 49
4.3.1 Results and Discussions . . . 49
4.4 Conclusions . . . 56
References . . . 56

Index . . . 59

About the Authors

Saumya Sengupta received his Bachelor of Science degree in Physics (Honours) from University of Calcutta, India, in 2006; Master of Science degree in Applied Physics from Indian School of Mines University, India, in 2008; and Ph.D. degree from Indian Institute of Technology Bombay, India, in 2014. He has been a postdoctoral research fellow with the Northwestern University, USA, from 2014 to 2016. His research interests include growth and characterization of novel III–V semiconductor materials by using Molecular beam epitaxy (MBE) and Metal-organic chemical vapor deposition (MOCVD) reactors for various opto-electronics applications. He is also involved in the characterization of optoelectronics devices. He has authored more than twenty international publications for various journals and conferences.

Subhananda Chakrabarti received his M.Sc. and Ph.D. degrees from the Department of Electronic Science, University of Calcutta, Kolkata, India, in 1993 and 2000, respectively. He was a Lecturer in the Department of Physics, St. Xavier's College, Kolkata. He has been a Senior Research Fellow at the University of Michigan, Ann Arbor, from 2001 to 2005; a Senior Researcher at Dublin City University, Dublin City, Ireland, from 2005 to 2006; and a Senior Researcher (RA2) at the University of Glasgow, Glasgow, UK, from 2006 to 2007. He joined as an Assistant Professor in the Department of Electrical Engineering, IIT Bombay, Mumbai, India, in 2007. Presently, he is a professor in the same department. He is a Fellow of the Institution of Electrical and Telecommunication Engineers (IETE), India, and also a Member of the IEEE, MRS USA, SPIE USA, etc. He is the 2016 medal recipient of the Materials Research Society of India and was also awarded the 2016 NASI-Reliance Industries Platinum Jubilee Award for application-oriented innovations in physical sciences. He serves as an Editor of the IEEE Journal of Electron Device Society. He has authored more than 250 papers in international journals and conferences. He has also co-authored a couple of book chapters on intersubband quantum dot detectors. Dr. S. Chakrabarti serves as a reviewer for a number of international journals of repute such as Applied Physics Letters, Nature

Scientific Reports, IEEE Photonics Technology Letters, IEEE Journal of Quantum Electronics, Journal of Alloys and Compound, Material Research Bulletin. His research interests lie in compound (III–V and II–VI) semiconductor-based opto-electronic materials and devices.

List of Figures

Fig. 1.1 Emission spectra of a blackbody at different temperatures 2
Fig. 1.2 Atmospheric infrared-light transmissions as a function of wavelength. 3
Fig. 1.3 Schematic representation of the density-of-states for **a** bulk material, **b** 1D, **c** 2D and **d** 3D confined nanostructure 5
Fig. 1.4 The differences between interband and intersubband energy transitions 5
Fig. 1.5 Schematic of different growth modes of epitaxial heterostructures 6
Fig. 1.6 Band gap and lattice constant of different semiconductors. 6
Fig. 1.7 Calculation of energy states inside an InAs/GaAs QDs heterostructure [25] 8
Fig. 2.1 Top view SEM images of dot distributions of samples 2106 and 2109. Reprinted from "Investigation of effect of varying growth pauses on the structural and optical properties of InAs/GaAs quantum dots heterostructure" Superlattices and Microstructures, Vol. 46, No. 4, pp. 611–617, October 2009 with permission from Elsevier 15
Fig. 2.2 STEM images of single QD grown at 0.032 ML/s with **a** 0 s and **b** 50 s of growth pause. Reprinted from "Investigation of effect of varying growth pauses on the structural and optical properties of InAs/GaAs quantum dots heterostructure" Superlattices and Microstructures, Vol. 46, No. 4, pp. 611–617, October 2009 with permission from Elsevier 15
Fig. 2.3 STEM images of single QD grown at 0.197 ML/s with **a** 0 s and **b** 50 s of growth pause. Reprinted from "Investigation of effect of varying growth pauses on the structural and optical properties of InAs/GaAs quantum dots heterostructure" Superlattices and Microstructures, Vol. 46, No. 4, pp. 611–617, October 2009 with permission from Elsevier 16

Fig. 2.4 PL-emission energies for samples 2106, 2105 and 2100 at 8 K. Reprinted from "Investigation of effect of varying growth pauses on the structural and optical properties of InAs/GaAs quantum dots heterostructure" Superlattices and Microstructures, Vol. 46, No. 4, pp. 611–617, October 2009 with permission from Elsevier 17
Fig. 2.5 PL-emission energies for samples 2109, 2108 and 2115 at 8 K. Reprinted from "Investigation of effect of varying growth pauses on the structural and optical properties of InAs/GaAs quantum dots heterostructure" Superlattices and Microstructures, Vol. 46, No. 4, pp. 611–617, October 2009 with permission from Elsevier 18
Fig. 2.6 Comparison of activation energies among the annealed counterparts of samples of all growth-pause durations 19
Fig. 2.7 Comparison of GS PL-emission peak of as-grown sample A, B and C and their annealed counterparts 19
Fig. 2.8 Comparison of the spectral response results of devices A and C at 50 K 21
Fig. 3.1 Schematic diagram of the BQD heterostructure. Reprinted from, "Effect of post-growth rapid thermal annealing on bilayer InAs/GaAs quantum dot heterostructure grown with very thin spacer thickness" Materials Research Bulletin, Vol. 45, No. 11, pp. 1593–1597, November 2010 with permission from Elsevier 27
Fig. 3.2 BFXTEM images of the InAs/GaAs BQD heterostructures—**a** 2044, **b** 2046 and **c** 2047. Reprinted from, "Vertical Ordering and Electronic Coupling in Bilayer Nanoscale InAs/GaAs Quantum Dots Separated by a Thin Spacer Layer", Nanotechnology, Vol. 19, p. 505704, December 2008 with permission from IOP Science. © IOP Publishing. Reproduced by permission of IOP Publishing. All rights 28
Fig. 3.3 BFXTEM images of sample A2046 **a** as-grown and annealed at **b** 700 °C and **c** 800 °C. Reprinted from, "Effect of post-growth rapid thermal annealing on bilayer InAs/GaAs quantum dot heterostructure grown with very thin spacer thickness" Materials Research Bulletin, Vol. 45, No. 11, pp. 1593–1597, November 2010 with permission from Elsevier 30

Fig. 3.4 Low-temperature (25 K) PL spectra of the three samples measured at an incident excitation power of 5 W/cm^2. Reprinted from, "Vertical Ordering and Electronic Coupling in Bilayer Nanoscale InAs/GaAs Quantum Dots Separated by a Thin Spacer Layer", Nanotechnology, Vol. 19, p. 505704, December 2008 with permission from IOP Science. © IOP Publishing. Reproduced by permission of IOP Publishing. All rights 31
Fig. 3.5 Low-temperature (25 K) PL spectra of the three samples measured at an incident excitation power of 500 W/cm^2. Reprinted from, "Vertical Ordering and Electronic Coupling in Bilayer Nanoscale InAs/GaAs Quantum Dots Separated by a Thin Spacer Layer", Nanotechnology, Vol. 19, p. 505704, December 2008 with permission from IOP Science. © IOP Publishing. Reproduced by permission of IOP Publishing. All rights 31
Fig. 3.6 Low-temperature (9 K) PL spectra from sample A2044, **a** as-grown and annealed at **b** 650 and **c** 700 °C. Reprinted from, "Effect of post-growth rapid thermal annealing on bilayer InAs/GaAs quantum dot heterostructure grown with very thin spacer thickness" Materials Research Bulletin, Vol. 45, No. 11, pp. 1593–1597, November 2010 with permission from Elsevier 33
Fig. 3.7 Low-temperature (9 K) PL spectra from sample A2046, as-grown and annealed at different temperatures. Reprinted from, "Effect of post-growth rapid thermal annealing on bilayer InAs/GaAs quantum dot heterostructure grown with very thin spacer thickness" Materials Research Bulletin, Vol. 45, No. 11, pp. 1593–1597, November 2010 with permission from Elsevier 34
Fig. 3.8 Arrhenius plot of the temperature dependence of the integrated PL for sample A2044 both as-grown and annealed at 700 °C. Reprinted from, "Effect of post-growth rapid thermal annealing on bilayer InAs/GaAs quantum dot heterostructure grown with very thin spacer thickness" Materials Research Bulletin, Vol. 45, No. 11, pp. 1593–1597, November 2010 with permission from Elsevier 35
Fig. 3.9 Arrhenius plot of the temperature dependence of the integrated PL for sample A2046, as-grown and annealed at 700 and 800 °C. Reprinted from, "Effect of post-growth rapid thermal annealing on bilayer InAs/GaAs quantum dot heterostructure grown with very thin spacer thickness" Materials Research Bulletin, Vol. 45, No. 11, pp. 1593–1597, November 2010 with permission from Elsevier 35

Fig. 3.10 Three-dimensional AFM images of SQD and BQD heterostructures. Reprinted from, "Comparison of single-layer and bilayer InAs/GaAs quantum dots with a higher InAs coverage", Opto-Electronics Review, Vol. 18, No. 3, pp. 295–299, September 2010 with permission from Springer 37
Fig. 3.11 Cross-sectional TEM images of different regions of the MQD heterostructure 38
Fig. 3.12 Comparison of SQD and BQD heterostructure PL spectra at 8 K. Reprinted from, "Comparison of single-layer and bilayer InAs/GaAs quantum dots with a higher InAs coverage", Opto-Electronics Review, Vol. 18, No. 3, pp. 295–299, September 2010 with permission from Springer 38
Fig. 3.13 Comparison of SQD and BQD heterostructure PL spectra at 300 K. Reprinted from, "Comparison of single-layer and bilayer InAs/GaAs quantum dots with a higher InAs coverage", Opto-Electronics Review, Vol. 18, No. 3, pp. 295–299, September 2010 with permission from Springer 39
Fig. 3.14 Comparison of SQD, BQD and MQD heterostructure PL spectra at 8 K 40
Fig. 3.15 Power-dependent PL spectra MQD heterostructure at 8 K. 40
Fig. 4.1 Schematic of the S–K growth mechanism 44
Fig. 4.2 Schematic design of the SML growth mode 45
Fig. 4.3 Low-temperature (8 K) PL spectra of samples with varying InAs thickness. Reprinted from, "A comprehensive study on molecular beam epitaxy-grown InAs sub-monolayer quantum dots with different capping combinations", J. Vac. Sci. Technol. B 31(3), 03C136-1, May/Jun 2013 with permission from AIP publishing LLC 46
Fig. 4.4 Low-temperature (8 K) PL spectra with varying GaAs barrier thickness. Reprinted from, "A comprehensive study on molecular beam epitaxy-grown InAs sub-monolayer quantum dots with different capping combinations", J. Vac. Sci. Technol. B 31(3), 03C136-1, May/Jun 2013 with permission from AIP publishing LLC 47
Fig. 4.5 Room-temperature PL spectra of samples A, B and C. Reprinted from, "A comprehensive study on molecular beam epitaxy-grown InAs sub-monolayer quantum dots with different capping combinations", J. Vac. Sci. Technol. B 31 (3), 03C136-1, May/Jun 2013 with permission from AIP publishing LLC 47

Fig. 4.6 Arrhenius plot from temperature-dependent PL experiments. Reprinted from, "A comprehensive study on molecular beam epitaxy-grown InAs sub-monolayer quantum dots with different capping combinations", J. Vac. Sci. Technol. B 31 (3), 03C136-1, May/Jun 2013 with permission from AIP publishing LLC 48
Fig. 4.7 Dark-current variation of devices A, B and C as a function of the applied bias voltage at 77 K. Reprinted from, "A comprehensive study on molecular beam epitaxy-grown InAs sub-monolayer quantum dots with different capping combinations", J. Vac. Sci. Technol. B 31(3), 03C136-1, May/Jun 2013 with permission from AIP publishing LLC 49
Fig. 4.8 PL spectra of device samples with a varying number of stacks at room temperature. 50
Fig. 4.9 Comparison of the PL for S–K- and SML-mode samples at room temperature. Reprinted from S. Sengupta et al., "Sub-monolayer quantum dots in confinement enhanced dots-in-a-well heterostructure", Applied Physics Letters, Vol. 100, p. 191111, 2012 with permission from AIP publishing LLC 50
Fig. 4.10 Comparison of normalized photocurrent spectra of QDIP devices with a varying number of stacks at 77 K. Reprinted from, "Multi-stack InAs/InGaAs sub-monolayer Quantum Dots Infrared Photodetectors", Applied Physics Letters, Vol. 102, p. 011131, 2013 with permission from AIP publishing LLC 51
Fig. 4.11 Detectivity as a function of the applied bias voltage for QDIP devices with a varying number of stacks at 77 K. Reprinted from, "Multi-stack InAs/InGaAs sub-monolayer Quantum Dots Infrared Photodetectors", Applied Physics Letters, Vol. 102, p. 011131, 2013 with permission from AIP publishing LLC 52
Fig. 4.12 Comparison of the normalized photocurrents of S–K and SML QDIPs at 77 K. Reprinted from S. Sengupta et al., "Sub-monolayer quantum dots in confinement enhanced dots-in-a-well heterostructure", Applied Physics Letters, Vol. 100, p. 191111, 2012 with permission from AIP publishing LLC 52
Fig. 4.13 Comparison of S–K- and SML-mode band structures. Reprinted from S. Sengupta et al., "Sub-monolayer quantum dots in confinement enhanced dots-in-a-well heterostructure", Applied Physics Letters, Vol. 100, p. 191111, 2012 with permission from AIP publishing LLC 53

Fig. 4.14 Dark current as a function of the applied bias voltage of QDIPs grown by S–K and SML growth modes, measured at 77 K 54
Fig. 4.15 Detectivity as a function of the applied bias voltage for S–K and SML QDIPs at 77 K. Reprinted from S. Sengupta et al., "Sub-monolayer quantum dots in confinement enhanced dots-in-a-well heterostructure", Applied Physics Letters, Vol. 100, p. 191111, 2012 with permission from AIP publishing LLC 54
Fig. 4.16 Responsivity as a function of applied bias voltage of S–K and SML QDIPS at 77 K. Reprinted from S. Sengupta et al., "Sub-monolayer quantum dots in confinement enhanced dots-in-a-well heterostructure", Applied Physics Letters, Vol. 100, p. 191111, 2012 with permission from AIP publishing LLC 55
Fig. 4.17 Gain and absorption efficiency as a function of the applied bias voltage at 77 K for S–K and SML QDIPs. Reprinted from S. Sengupta et al., "Sub-monolayer quantum dots in confinement enhanced dots-in-a-well heterostructure", Applied Physics Letters, Vol. 100, p. 191111, 2012 with permission from AIP publishing LLC 55

List of Tables

Table 1.1 Band gap and corresponding wavelengths of common semiconductors 4
Table 3.1 Details of different InAs/GaAs BQD heterostructure samples 27

Abbreviations

0D	Zero-dimensional
1D	One-dimensional
2D	Two-dimensional
3D	Three-dimensional
A	Ampere
Å	Angstrom
AFM	Atomic force microscopy
Al	Aluminium
As	Arsenic
Au	Gold
BEP	Beam equivalent pressure
BF	Bright field
BQD	Bilayer quantum dot
CCD	Charge-coupled device
CE	Confinement enhancing
cm	Centimetre
D	Detectivity
D*	Specific detectivity
DC	Direct current
DI	De-ionized
DOS	Density of states
EM	Electromagnetic
FFT	Fast Fourier transform
FTIR	Fourier transform infrared spectroscopy
FWHM	Full width at half maximum
Ga	Gallium
Ge	Germanium
gm	Gram
G-R	Generation-recombination
HAADF	High-angle annular dark field

HgCdTe/MCT	Mercury Cadmium Telluride
HNO_3	Nitric acid
H_2O	Hydrogen monoxide, water
H_2O_2	Hydrogen peroxide
H_3PO_4	Phosphoric acid
HRTEM	High-resolution transmission electron microscopy
Hz	Hertz
IIT	Indian Institute of Technology
In	Indium
IPA	Isopropyl alcohol
IR	Infrared
K	Kelvin
keV	Kilo electron volt
kV	Kilo volt
LCC	Leaded chip carrier
LN_2	Liquid nitrogen
LO	Longitudinal optical
LWIR	Long-wavelength infrared
MBE	Molecular beam epitaxy
MCT	Mercury Cadmium Telluride
MeV	Mega electron volt
MOCVD	Metal organic chemical vapour deposition
meV	Milli electron volt
mJ	Milli Joules
ML	Monolayer
mm	Millimetre
Mo	Molybdenum
MQD	Multilayer quantum dot
mW	Milliwatt
MWIR	Mid-wavelength infrared
μm	Micrometre
N_2	Nitrogen
NEP	Noise equivalent power
Ni	Nickel
nm	Nanometre
PC	Photoconductive gain
PID	Proportion, integral and derivative
PL	Photoluminescence
PPR	Positive photoresist
QD	Quantum dot
QDIP	Quantum dot infrared photodetector
QMS	Quadrupole mass spectrometer
QW	Quantum well
QWIP	Quantum well infrared photodetectors
R	Responsivity

RHEED	Reflection high-energy electron diffraction
Sb	Antimony
Si	Silicon
S-K	Stranski–Krastanov
SML	Sub-monolayer
SNR	Signal-to-noise ratio
SQD	Single-layer quantum dot
STEM	Scanning transmission electron microscopy
TCE	Trichloroethylene
TEM	Transmission electron microscopy
TSP	Titanium sublimation pump
W	Watt
XTEM	Cross-sectional transmission electron microscopy

Chapter 1
Introduction to Infrared Detectors and Quantum Dots

Abstract The majority of objects, those with a temperature between 100 and 400 K, emit strong electromagnetic radiation in the infrared region, especially in 1–14 μm region, which includes short-wavelength infrared (SWIR, ∼1.0–3.0 μm), medium-wavelength infrared (MWIR, ∼3.0–5.0 μm), long-wavelength infrared (LWIR, ∼8.0–14.0 μm) and some part of very-long infrared (VLWIR, ∼14.0–100.0 μm). MWIR and LWIR detectors are widely used today in a variety of imaging and video-graphic applications, in fields such as spectroscopy, night vision, thermal imaging, health science, and space research and defence. Different types of IR detectors are based on various semiconductor materials, such as Si, $InAs_{1-x}Sb_x$, $Pb_{1-x}Sn_xTe$, and $Hg_{1-x}Cd_xTe$. To overcome limitations in extending the detection wavelength in longer wavelength region the idea of intersubband transition based photodetectors has been introduced. The spacing between different electronics subbands (a few tenths to hundreds of meV) allows emission or detection of a broad range of IR radiation. Quantum mechanical properties dictate that if any material is scaled down to very small dimension both the conduction and valence band can be split into a number of intersubband energy levels. The dimension of the bulk can be reduced to form different nanostructures, such as quantum wells (QWs), quantum wires and quantum dots (QDs). QDs confine the carriers in all three directions, which results in a complete delta-like DOS in the different energy levels. In recent past MBE grown III–V semiconductors based quantum dots infrared photodectors (QDIPs) have emerged as a potential candidate in the field of MWIR and LWIR imaging technology. Their 3-D carrier confinement provides intrinsic sensitivity to normal incidence radiation, lower dark current and a long excited-state lifetime compared to quantum well infrared photodetectors (QWIPs).

Keywords Infrared photodetector · Quantum dots · Molecular beam aepitaxy

© Springer Nature Singapore Pte Ltd. 2018

S. Sengupta and S. Chakrabarti, *Structural, Optical and Spectral Behaviour of InAs-based Quantum Dot Heterostructures*,
DOI 10.1007/978-981-10-5702-1_1

1.1 Introduction and Evolution of IR Detectors

A detector is a device able to sense a signal from its surroundings. Detectors exist for various types of input signal, which can be mechanical vibration, electromagnetic radiation, small particles and other physical phenomena. A photodetector is a sensor that detects electromagnetic (EM) waves and converts them into a measurable output signal, such as electrical current or voltage. A large variety of photodetectors, based on different materials and technologies, suit a variety of specific purposes [1–7].

The region in the wavelengths between ~0.74 and 100.0 μm is known as the infrared (IR) region. The IR region is divided into different windows, such as near infrared (NIR, ~0.74–1.0 μm), short-wavelength infrared (SWIR, ~1.0–3.0 μm), medium wavelength infrared (MWIR, ~3.0–5.0 μm), long-wavelength infrared (LWIR, ~8.0–14.0 μm) and very long infrared (VLWIR, ~14.0–100.0 μm).

In 1901, Max Planck described the emission of EM radiation from a black body source with the variation in temperature. He formulated an equation which measures the amount of EM radiation emitted by a blackbody source at different temperatures [8]. Total energy density of black body radiation is given by

$$U(v,T) = \frac{8\pi h}{c^3} \int_0^\infty \frac{v^3 \mathrm{d}v}{\mathrm{e}^{hv/kT} - 1} \text{ (Energy/volume/spectral unit)}$$

where c, h, v, k, T are speed of light, Planck's constant, frequency of radiation of the blackbody, Boltzmann's constant and absolute temperature of the black body respectively.

This theoretical equation, which is known as Planck's law, has a good agreement with experimental results. The variation of the emitted photon flux as a function of

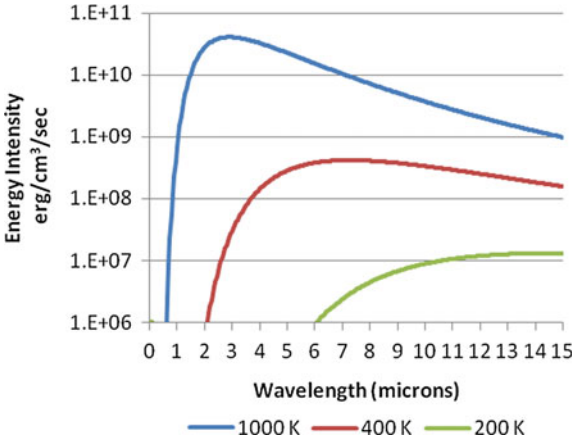

Fig. 1.1 Emission spectra of a blackbody at different temperatures

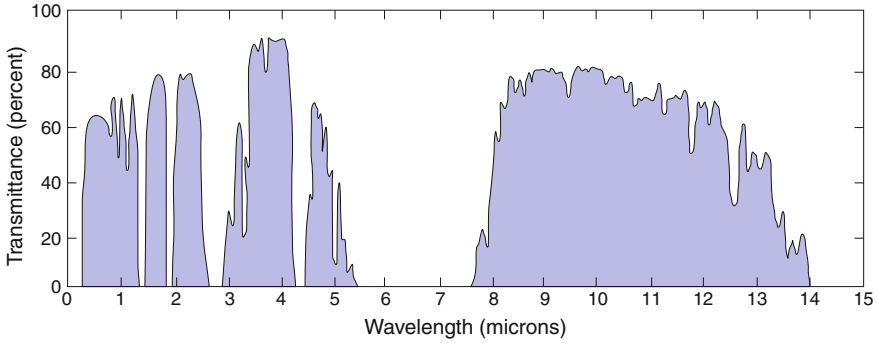

Fig. 1.2 Atmospheric infrared-light transmissions as a function of wavelength

temperature of the black body is shown in Fig. 1.1 It shows that the majority of objects with a temperature 400 K emit strong EM radiation in the infrared region, especially in the region of 1–14 μm.

But the transmittance of EM energy through the atmosphere varies significantly for different wavelengths. There are convenient windows in IR region where atmospheric absorption is minimal. Two of these transmission windows fall in the MWIR and LWIR bands (Fig. 1.2) [9]; MWIR and LWIR detectors find wide application in a variety of imaging and video-graphics applications, in fields such as spectroscopy, night vision, thermal imaging, health science, space research and defence.

IR detectors are divided into two broad categories [10, 11]. The first category is thermal detectors. A thermal detector absorbs incident radiation in the form of heat. The heat changes the material temperature of the device, altering its physical properties and producing an electrical output. The other category produces an output signal resulting from change in its electrical properties when it absorbs incident radiation in form of energy. While photodetectors usually require a low-temperature environment for best performance, thermal detectors can operate at room temperature though they tend to suffer from low sensitivity and slow response times.

IR detectors became popular in the 1950s in defence applications. The availability of incorporating controlled-doping technology in semiconductors, allowed use of extrinsic photoconductive detectors specially for LWIR and VLWIR, followed by the development of Si-based charge-coupled detectors (CCD). The introduction of semiconductor alloys, such as III–V ($InAs_{1-x}Sb_x$, $InGa_{1-x}As_x$), IV–VI ($Pb_{1-x}Sn_xTe$), II–VI ($Hg_{1-x}Cd_xTe$) etc. materials, in the 1960s changed the scenario significantly. These materials provide the ability to tune the detection wavelength over a broad range by engineering its band gap. In 1973, metal silicide/silicon Schottky-barrier detectors were introduced which had the advantage of being compatible with advanced chip based electronic readout system [11]. Photodetectors based on HgCdTe (MCT) dominate IR imaging technology; however they suffer from serious disadvantages, including high dark current caused by

Table 1.1 Band gap and corresponding wavelengths of common semiconductors

Semiconductor material	Band gap at 300 K (eV)	Wavelength, λ_c (μm)
InSb	0.17	7.29
InAs	0.36	3.44
Ge	0.66	1.88
GaSb	0.72	1.72
Si	1.12	1.11
InP	1.35	0.92
GaAs	1.42	0.87
CdTe	1.56	0.79

band-to-band carrier tunnelling. Other problematic issues relate to the health hazard the material creates and growth-related problems, such as the difficulty of obtaining uniform composition of material for large wafers, softness of the grown material and difficulty in controlling the compositional stoichiometry.

Table 1.1, which shows the threshold wavelength of popular semiconductors, makes it clear that there are few options for MWIR and LWIR imaging based on the band-to-band transition principle. Current research examines the idea of intersubband transition-based photodetectors as a way of extending the detection wavelength.

1.2 Introduction to Quantum Dots

Quantum mechanics dictates that, if any material is scaled down to small dimensions both the conduction and valence band can be split into a number of closely-spaced discrete-energy levels, known as intersubbands. The dimension of the bulk can be reduced to form different nanostructures, such as the quantum well (QW), quantum wire and quantum dot (QD) with different degrees of carrier confinement inside the structure. The reduction in dimension also alters the equation of density-of-states (DOS) of different energy levels as shown in Fig. 1.3.

Figure 1.4 shows the comparison between interband and intersubband transitions. In this figure different subbands within conduction band (E_{C1}, E_{C2}) and valance band (E_{V1}, E_{V2}) are schematically shown. The energy spacing of intersubband levels is much smaller than the same of interband levels. Such nanostructures of suitable material and sample-design, and the transition between their intersubbands allow extending the detection wavelength into the desired MWIR LWIR and limited range of VLWIR regimes.

Drastic improvements in epitaxial-growth techniques, such as Molecular beam epitaxy (MBE) and Metal-organic chemical vapor deposition (MOCVD), over the last decades have accelerated research into nanostructure semiconductors. In quantum dots, carriers are confined in all three directions, which results in complete delta-like DOS in the different energy levels. In 1982, Arakawa and Sakaki predicted that the performance of semiconductor lasers could be improved by reducing

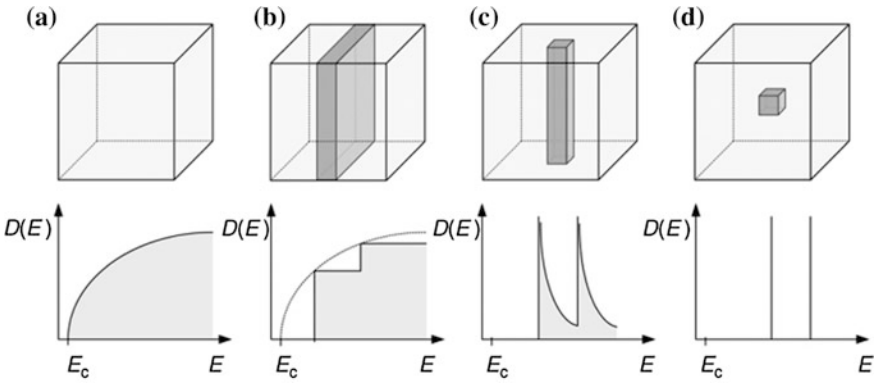

Fig. 1.3 Schematic representation of the density-of-states for **a** bulk material, **b** 1D, **c** 2D and **d** 3D confined nanostructure

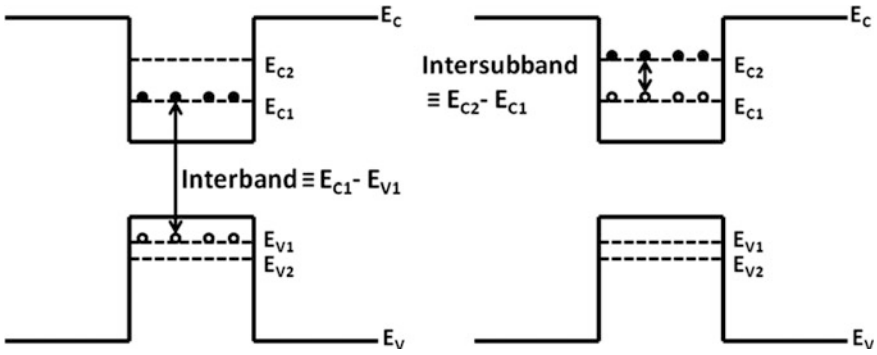

Fig. 1.4 The differences between interband and intersubband energy transitions

the dimensionality of their active regions. Several approaches lend themselves to practical QD fabrication, including ultrafine-lithographic techniques, pulsed-laser annealing and ion implantation, chemical methods and selective epitaxial deposition on patterned substrates. This research work focuses on III–V semiconductor-based, self-assembled QDs using the Stranski-Krastanov (S–K) growth mechanism [12–16].

Figure 1.5 shows the three types of heteroepitaxial growth mechanisms. Each results in a complicated combination of strains due lattice mismatches and surface kinetics between the substrate and deposited layer materials.

Where the materials have very little lattice mismatch between them (e.g., AlGaAs/GaAs), layer-by-layer formation occurs, governed solely by the surface and interface energies of the substrate and deposited epilayer materials. In this case, the sum of the epilayer surface energy and interface energy is lower than the surface energy of the substrate. This is the Frank-van der Merwe growth mode

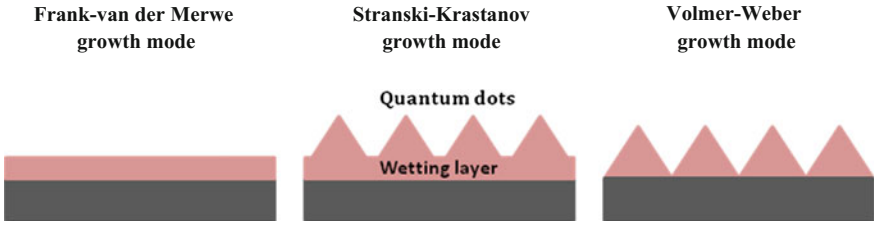

Fig. 1.5 Schematic of different growth modes of epitaxial heterostructures

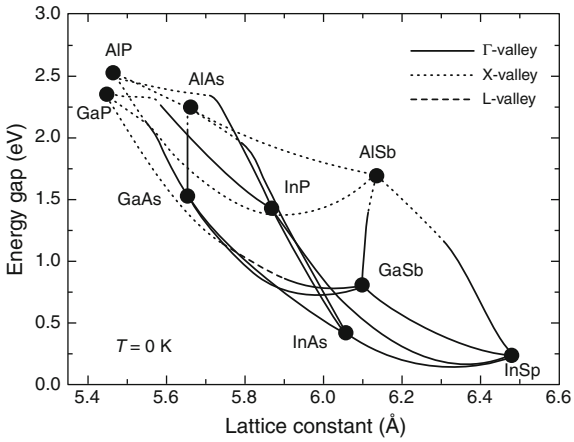

Fig. 1.6 Band gap and lattice constant of different semiconductors

[17]. In this case growth initiates with a 2D-nucleation process, where monolayers (ML) form on the surface, with each layer completing before the next forms. The opposite situation occurs in Volmer-Weber growth, where an extreme lattice mismatch exists (higher than 12%) and the sum of the epilayer surface energy and interface energy is higher than the surface energy of the substrate [18]. As a result, the deposited epilayer directly forms large 3D island on the top of substrate layer. The S–K growth mode is the intermediate case, with moderate lattice mismatch in the materials ($\sim$2.0–10.0%). During this process, initially forms a 2D layer known as the wetting layer. As monolayers of material are deposited, strain builds up gradually in the system due to the lattice mismatch, increasing the surface energy. After exceeding the critical thickness, self-assembled 3D islands or dots are formed, leading to a minimization in the system's surface. The term *self-assembled* refers to the spontaneous nature of formation of islands. Materials can be chosen according to the lattice mismatch-compatibility of the epitaxial heterostructure growth method and requirements, as shown in Fig. 1.6 [19]. Most of the work reported in the thesis report is based on S–K growth mode grown self-assemble InAs/GaAs QDs with a $\sim$7.0% lattice mismatch.

The physics of the structural analysis and electronics properties of QD under S–K growth mechanism are not completely understood. A detailed analysis is beyond the scope of this publication, however, we will touch briefly on few points related to this research [20, 21].

Theoretically, to achieve complete 3D carrier confinement, the nanostructure should have dimensions less than the Bohr radii of the carriers. In practice, for the heterostructure under consideration (a type I heterostructure) the minimum diameter $D_{\min}$. of the dots is the minimum size required to accommodate at least one electronic energy level, and can be estimated as follows:

$$D_{\min} = \frac{h}{2\sqrt{\left(2m_e^* \Delta E_c\right)}}$$

where $D_{\min}$ minimum diameter, m_e^* the effective is mass of the electron and ΔE_c is the electron-confinement width. The maximum dot size can be estimated by the argument restricting the thermal population of higher-energy subbands, which are undesirable for devices such as interband lasers and intersubband detectors. The condition for limiting the thermal population of higher-energy levels to 5% (i.e., $\sim e^{-3}$) can be written as follows:

$$kT \leq \frac{1}{3}(E_1 - E_2)$$

where E_1, E_2 are the energies of the first and second electronic states, respectively.

Models have been proposed to explain the strain distribution in QDs, such as the continuum-mechanical model [22], valence force-field model [23] and density-functional techniques [24]. The valance force-field (VFF) model has shown good agreement with experimental results. According to this model, strain distribution has highest degree of relaxation at the top of the dot and gradually increases towards the bottom. The electronic structure of a 3D-confinement system under strain conditions is very complex and different than its bulk counterpart. A strain tensor with strong spatial variation significantly affects the electronics properties of such low-dimensional structure. For example, the band gap of bulk InAs is 0.4 eV while the effective band gap of a self-assembled InAs dot is $\sim$1.1 eV. Jiang and Singh calculated the electronic band levels using the 8-band k·p model, taking the influence of remote bands on the conduction and valence band states into account [25]. In the presence of strain, the Hamiltonian has the following form:

$$H_t = H_0 + H_{\text{str}}$$

where H_0 and H_{str} are the kinetic and strain components, respectively.

The band structure depends on the size and shape of the dots. For pyramidal InAs/GaAs QDs with a base width of 124 Å and height of 64 Å, the electronic spectrum is solved using the 8-band k.p model (Fig. 1.7). A number of excited states can exist in the conduction and valance band. Simple optical experiments, such as photoluminescence with adequate excitation power, easily confirm the presence of

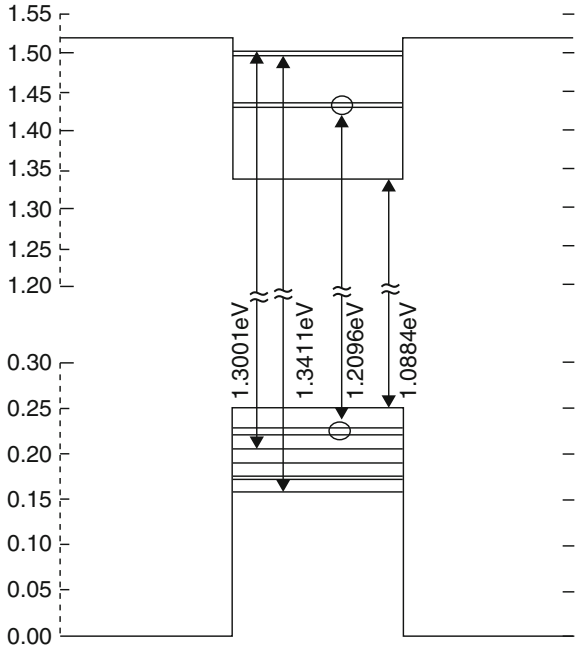

Fig. 1.7 Calculation of energy states inside an InAs/GaAs QDs heterostructure [25]

excited states. It should be noted that one of the most critical factors in obtaining electronic structure of QDs heterostructure is effective mass of carriers. Effective mass of both electrons and holes have huge variation with strain in the system [26].

We have already discussed the complicated nature of strain profile in QDs; therefore it's extremely difficult to accurately predict the electronic band structure theoretically. Nevertheless, some existing modelling works based on extensive theoretical calculations are capable to depict the electronics properties to a good extend. Figure 1.7 shows that the difference between the ground state and the first excited state in the conduction band is $\sim$62 meV. There are also many confined-hole states. The splitting between the ground and excited-hole states ranges from 22 to 30 meV. Because the intersubband spacing is larger than the optical phonon energy in GaAs (36 meV), optical phonon scattering, which constitutes the major scattering mechanism in quantum wells, is suppressed in the dots. This prevents carriers in the excited state from relaxing to the ground state. This effect is referred to as a *phonon bottleneck* [27].

1.3 Motivation and Objective of the Work

QDIP based technology has emerged as a potential candidate for next generation IR imaging technology over the last decade [28–31]. 3D carrier confinement provides quantum dot infrared photodetectors (QDIPs) many advantages over quantum well infrared photodetectors (QWIPs) and MCT based photodetectors [32–34]:

1. QWIPs allow only transitions polarized perpendicular to the growth direction, due to absorption-selection rules. The selection rules in QDIPs are inherently different, and absorption of radiation with random polarization is observed. This advantage has made the fabrication process of QDIP device significantly easier compared to the QWIP as it doesn't require employment of grating.
2. As generation by longitudinal optical (LO) phonons is prohibited due to *phonon bottleneck* effect thermal generation of electrons is significantly reduced. The *phonon bottleneck* enables photo-excited carriers that are generated in an intersubband detector to live longer in the excited state and, thus, increases the probability of photo-excited carriers getting swept out as photocurrent.
   In quantum wells, since the levels are quantized only in the growth direction and a continuum exists in the other two, hence generation-recombination by LO phonons is possible with capture time of few picoseconds.
3. QDIPs are expected to exhibit lower dark current than MCT detectors and QWIPs due to 3D quantum confinement of the electron wave-function.
4. Availability of mature growth and fabrication technology in larger format for QDIPs is another advantage over the MCT based photodetector technology.

The main disadvantages of the QDIPs are *self-assembled* nature of formation of dots and the presence of wetting layer. Random formation of dots induces inhomogeneous linewidth in the QD emission peak. Defects such as Gr-III vacancies and interstitials generally provide additional non-radiative channels in confined structures that quench luminescence. The occurrence of vacancies and interstitials are natural at the interface between the QDs and the GaAs barrier because of the generation of strain due to lattice mismatch epitaxy of InAs/GaAs. Presence of such defects degrades the quality of the sample drastically. Thermal annealing is amongst post-growth treatments which helps dissolve such defects and enhances the optical quality of the sample. Under optimum thermal energy, mass redistribution occurs in QDs, which may improve the uniformity of dot size. So the quality of QDs can be improved by using rapid thermal annealing (RTA) treatment [35–41]. Formation of wetting layer can be avoided by deploying a different growth mode than conventional S–K-sub-monolayer (SML) growth technique. Since the size of the dots grown under this mode is much smaller compared to S–K mode and has no wetting layer, the electronics behaviour is expected to improve significantly.

Motivated by opportunities for performance improvements, we carried out intensive research on QDIPs grown with solid-state MBE using InAs/(In)(Al)GaAs semiconductor materials on GaAs substrate. Considerable time was devoted to optical and structural characterization of QDs in different heterostructures. We also investigated the possibility of enhancing QD quality through post-growth treatment, such as rapid-thermal annealing and examined the fabrication and characterization of high-performance QDIPs. Along with the QDIP grown with the S–K growth mode, we explored sub-monolayer growth techniques and established its superiority to S–K.

1.4 Conclusion

In conclusion, the first chapter deals with the basics of infrared photodetectors and their evolution over time. It introduces the general properties of semiconductor QDs, followed by the motivations for carrying out this research.

References

1. M.A. Khan, J. Kuznia, D. Olson, M. Blasingame, A. Bhattarai, Schottky barrier photodetector based on Mg-doped p-type GaN films. Appl. Phys. Let. **63**, 2455–2456 (1993)
2. J. Law, J. Thong, Simple fabrication of a ZnO nanowire photodetector with a fast photoresponse time. Appl. Phys. Let. **88**, 133114 (2006)
3. A. Poglitsch, C. Waelkens, N. Geis, H. Feuchtgruber, B. Vandenbussche, L. Rodriguez et al., The photodetector array camera and spectrometer (PACS) on the Herschel space observatory. arXiv preprint arXiv:1005.1487 (2010)
4. L. Vivien, J. Osmond, J.-M. Fédéli, D. Marris-Morini, P. Crozat, J.-F. Damlencourt et al., 42 GHz pin germanium photodetector integrated in a silicon-on-insulator waveguide. Opt. Express **17**, 6252–6257 (2009)
5. F. Xia, T. Mueller, Y.-M. Lin, A. Valdes-Garcia, P. Avouris, Ultrafast graphene photodetector. Nat. Nanotechnol. **4**, 839–843 (2009)
6. A.W. Hoffman, P.J. Love, J.P. Rosbeck, Megapixel detector arrays: visible to 28 μm, in Optical science and technology, SPIE's 48th annual meeting, (2004), pp. 194–203
7. D. Smith, C. Mailhiot, Proposal for strained type II superlattice infrared detectors. J. Appl. Phys. **62**, 2545–2548 (1987)
8. M. Planck, On the law of distribution of energy in the normal spectrum. Ann. Phys. **4**, 1 (1901)
9. Available: http://en.wikipedia.org/wiki/Infrared
10. A. Rogalski, Infrared detectors: an overview. Infrared Phys. Technol. **43**, 187–210 (2002)
11. A. Rogalski, Infrared detectors: status and trends. Prog. Quant. Electron. **27**, 59–210 (2003)
12. H. Drexler, D. Leonard, W. Hansen, J. Kotthaus, P. Petroff, Spectroscopy of quantum levels in charge-tunable InGaAs quantum dots. Phys. Rev. Let. **73**, 2252 (1994)
13. R. Heitz, M. Veit, N.N. Ledentsov, A. Hoffmann, D. Bimberg, V.M. Ustinov et al., Energy relaxation by multiphonon processes in InAs/GaAs quantum dots. Phys. Rev. B **56**, 10435 (1997)
14. D. Leonard, K. Pond, P. Petroff, Critical layer thickness for self-assembled InAs islands on GaAs. Phys. Rev. B **50**, 11687 (1994)
15. G. Solomon, J. Trezza, J. Harris Jr., Substrate temperature and monolayer coverage effects on epitaxial ordering of InAs and InGaAs islands on GaAs. Appl. Phys. Let. **66**, 991–993 (1995)
16. Q. Xie, P. Chen, A. Kalburge, T. Ramachandran, A. Nayfonov, A. Konkar et al., Realization of optically active strained InAs island quantum boxes on GaAs (100) via molecular beam epitaxy and the role of island induced strain fields. J. Cryst. Growth **150**, 357–363 (1995)
17. F. Frank, J.H. van der Merwe, One-dimensional dislocations. I. static theory, in *Proceedings of the Royal Society of London. Series A. Mathematical and Physical Sciences*, vol. 198 (1949), pp. 205–216
18. M. Volmer, A. Weber, Keimbildung in übersättigten Gebilden. Z. Phys. Chem. **119**, 277–301 (1926)
19. I. Vurgaftman, J. Meyer, L. Ram-Mohan, Band parameters for III–V compound semiconductors and their alloys. J. Appl. Phys. **89**, 5815–5875 (2001)
20. D. Bimberg, M. Grundmann, N.N. Ledentsov, *Quantum Dot Heterostructures*, vol. 471973882 (John Wiley Chichester, 1999)

21. S. Krishna, Optoelectronics properties of self-assembled InAs/InGaAs quantum dots. III-V Semicond Heterostruct Phys Devices **3438**, 234–242 (2003)
22. A. Sada, *Elasticity: Theory and Application* (ed: Pergamon Press, 1974)
23. P. Keating, Theory of the third-order elastic constants of diamond-like crystals. Phys. Rev. **149**, 674 (1966)
24. M. Scheffler, J.P. Vigneron, G.B. Bachelet, Total-energy gradients and lattice distortions at point defects in semiconductors. Phys. Rev. B **31**, 6541 (1985)
25. H. Jiang, J. Singh, Self-assembled semiconductor structures: electronic and optoelectronics properties. Quantum Electron. IEEE J. **34**, 1188–1196 (1998)
26. J. Singh, *Electronic and Optoelectronics Properties of Semiconductor Structures* (Cambridge University Press, Cambridge, 2003)
27. U. Bockelmann, T. Egeler, Electron relaxation in quantum dots by means of Auger processes. Phys. Rev. B **46**, 15574 (1992)
28. P. Bhattacharya, X. Su, S. Chakrabarti, G. Ariyawansa, and A. Perera, Characteristics of a tunneling quantum-dot infrared photodetector operating at room temperature. Appl. Phys. Lett. **86**, 191106–191106-3 (2005)
29. H. Lim, S. Tsao, W. Zhang, M. Razeghi, High-performance InAs quantum-dot infrared photodetectors grown on InP substrate operating at room temperature. Appl Phys Lett. **90**, 131112–131112-3 (2007)
30. X. Su, S. Chakrabarti, P. Bhattacharya, G. Ariyawansa, A.U. Perera, A resonant tunneling quantum-dot infrared photodetector. Quantum Electron. IEEE J. **41**, 974–979 (2005)
31. S. Tsao, H. Lim, H. Seo, W. Zhang, M. Razeghi, InP-based quantum-dot infrared photodetectors with high quantum efficiency and high-temperature imaging. Sens. J. IEEE **8**, 936–941 (2008)
32. U. Bockelmann, G. Bastard, Phonon scattering and energy relaxation in two-, one-, and zero-dimensional electron gases. Phys. Rev. B **42**, 8947 (1990)
33. D. Pan, E. Towe, S. Kennerly, Normal-incidence intersubband (In, Ga) As/GaAs quantum dot infrared photodetectors. Appl. Phys. Lett. **73**, 1937–1939 (1998)
34. A. Stiff, S. Krishna, P. Bhattacharya, S. Kennerly, High-detectivity, normal-incidence, mid-infrared ($\lambda \sim 4$ μm) InAs/GaAs quantum-dot detector operating at 150 K. Appl. Phys. Lett. **79**, 421–423 (2001)
35. A. Tartakovskii, M. Makhonin, I. Sellers, J. Cahill, A. Andreev, D. Whittaker et al., Effect of thermal annealing and strain engineering on the fine structure of quantum dot excitons. Phys. Rev. B **70**, 193303 (2004)
36. H. Lee, J. Lee, T. Kim, M. Kim, Effect of thermal annealing on the microstructural and optical properties of vertically stacked InAs/GaAs quantum dots embedded in modulation-doped heterostructures. J. Appl. Phys. **94**, 6354–6357 (2003)
37. S. Xu, X. Wang, S. Chua, C. Wang, W. Fan, J. Jiang et al., Effects of rapid thermal annealing on structure and luminescence of self-assembled InAs/GaAs quantum dots. Appl. Phys. Lett. **72**, 3335–3337 (1998)
38. C. Chia, S. Chua, Z. Miao, Y. Chye, Enhanced photoluminescence of InAs self-assembled quantum dots grown by molecular-beam epitaxy using a "nucleation-augmented" method. Appl. Phys. Lett. **85**, 567–569 (2004)
39. W. Lu, Y. Ji, G. Chen, N. Tang, X. Chen, S. Shen et al., Enhancement of room-temperature photoluminescence in InAs quantum dots. Appl. Phys. Lett. **83**, 4300–4302 (2003)
40. S. Fafard, C.N. Allen, Intermixing in quantum-dot ensembles with sharp adjustable shells. Appl. Phys. Lett. **75**, 2374–2376 (1999)
41. T. Hsu, Y. Lan, W.-H. Chang, N. Yeh, J.-I. Chyi, Tuning the energy levels of self-assembled InAs quantum dots by rapid thermal annealing. Appl. Phys. Lett. **76**, 691–693 (2000)

Chapter 2
Structural, Optical and Spectral Characterization of Single-Layer QDIPs

Abstract In this chapter, we have investigated the effect of growth pause on structural, optical and spectral properties of InAs/GaAs QD materials. Introduction of growth pause or ripening time changes the morphology of the QDs by altering effective epitaxial strain during the growth of QDs. Initially, we grew single-layer QD samples, with another QD layer on the top of the surface for structural characterization. Sample sets with two different InAs growth rates (0.032 and 0.197 ML/s) were grown on (100)-oriented GaAs substrates. Three samples, with 0, 25 and 50 s growth pause, were grown with each of the two growth rates, keeping all other growth parameters constant. We have examined the change of their optical and structural properties with different duration of growth pause. For device fabrication, we grew 10 mutually uncoupled QD layers sandwiched between Si-doped thick GaAs contact layers. In this case, the InAs dots were grown at 520 °C with a growth rate of 0.1 MLs^{-1}. Growth pauses of 0, 25 and 50 s were introduced for samples A, B and C, respectively. Finally, single-pixel photodetector devices were fabricated from as-grown A, B and C samples with standard fabrication procedures.

Keywords Growth pause · Scanning electron microscope · Photoluminescence

2.1 Introduction[1]

In recent past, InAs/GaAs-based self-assembled QD heterostructures have drawn a great deal of attention from scientific community, especially in the field of optoelectronic devices such as laser, photodetector [1–6]. The performance of any such device depends upon its dot density, dot size and the uniformity of dot-size distribution. All of

[1]Reprinted from "Presentation and experimental validation of a model for the effect of thermal annealing on the photoluminescence of self-assembled InAs/GaAs quantum dots", Journal of Applied Physics, vol. 107, pp. 123107, Jun. 2010 with permission from AIP publishing LLC. and

Reprinted from "Investigation of effect of varying growth pauses on the structural and optical properties of InAs/GaAs quantum dots heterostructure" Superlattices and Microstructures, Vol. 46, No. 4, pp. 611–617, October 2009 with permission from Elsevier.

© Springer Nature Singapore Pte Ltd. 2018

S. Sengupta and S. Chakrabarti, *Structural, Optical and Spectral Behaviour of InAs-based Quantum Dot Heterostructures*,
DOI 10.1007/978-981-10-5702-1_2

these characteristics depend on the optimization of growth parameters, such as the InAs growth rate, growth temperature, thickness of the InAs monolayer (ML), V/III ratio of the flux [7, 8]. It is a usual practice to grow single-layer QD heterostructures for optimization of different growth parameters. Another very important, but relatively less investigated parameter is the growth pause or ripening pause during the growth of the sample [9]. The growth pause is defined as the time interval between the end of QD deposition and subsequent deposition of the barrier. In the S–K growth mode, the formation of QDs is driven by the mass transport under partially strained condition, as the deposited layer (InAs) exceeds a certain critical thickness. The grown InAs QDs always have a tendency to interact with neighbouring QDs through the substrate under epitaxially strained condition. When delaying covering the QDs, i.e. introducing a growth pause, QDs are allowed to relax in an energetically favourable condition, as well as to interact with the surrounding QDs for longer time. QDs under such conditions show a ripening behaviour. So introduction of growth pause can effectively alter the morphology of the sample. In this work, we have investigated the effect of growth pause on single-layer InAs/GaAs QD heterostructures. We have grown two sets of sample - 1st set has three samples namely 2106, 2105 and 2100 with 0, 25 and 50 s of growth interruption respectively. These three samples were grown at the growth rate of 0.032 ML/s. The other set which has another three samples - 2109, 2108 and 2115 with 0, 25 and 50 s of growth interruption was grown at 0.197 ML/s growth rate. Two different growth rates were chosen to study the effect of growth rate on the morphology of the sample.

The later part of the work studied effect of thermal treatment on the sample. Rapid thermal annealing (RTA) of QD heterostructures at temperatures 600–800 °C is a popular post-growth treatment [10–15]. It is believed that RTA leads to a relatively homogenized size distribution in the QD ensemble, a relaxed strain distribution and a reduction in structural defects, thereby improving the optical properties of the sample [16–18]. We also investigated the effects of RTA on the optical properties of the QD samples with growth pauses at different temperatures.

2.2 Results and Discussion

2.2.1 Structural Characterization

Figure 2.1 shows the SEM images of samples grown with slow (#2106) and fast (#2109) deposition rates. The average dot density is 0.6×10^{10} dots per cm^2 and from 2.3×10^{10} dots per cm^2 for slow and fast growth-rate samples, respectively. Faster deposition helps produce a higher dot density due to the competition between the nucleation rate and nucleation probability.

For a lower growth rate, the growth process is dominated by the nucleation probability. The nucleation rate increases with the increment in growth rate, resulting in a higher dot density. At a very fast growth rate, the nucleation rate and nucleation probability reach a dynamic equilibrium, resulting in dot-density saturation [19].

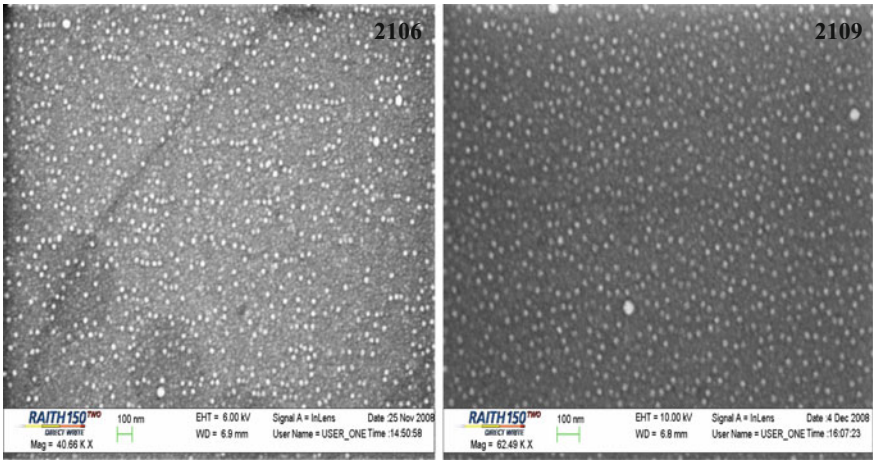

Fig. 2.1 Top view SEM images of dot distributions of samples 2106 and 2109. Reprinted from "Investigation of effect of varying growth pauses on the structural and optical properties of InAs/GaAs quantum dots heterostructure" Superlattices and Microstructures, Vol. 46, No. 4, pp. 611–617, October 2009 with permission from Elsevier

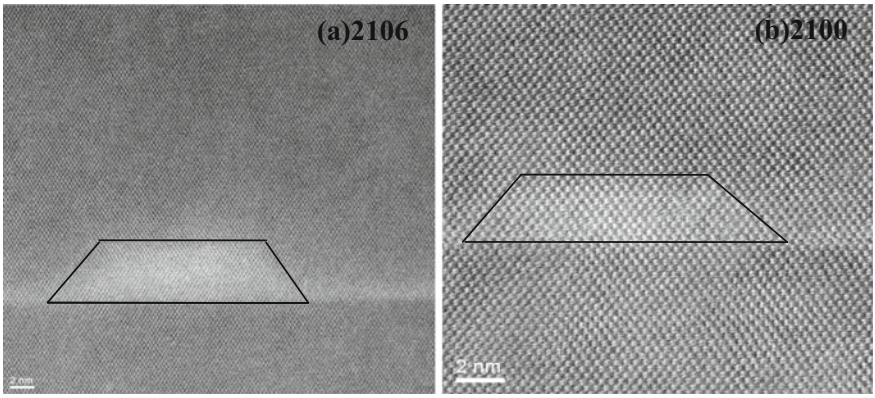

Fig. 2.2 STEM images of single QD grown at 0.032 ML/s with **a** 0 s and **b** 50 s of growth pause. Reprinted from "Investigation of effect of varying growth pauses on the structural and optical properties of InAs/GaAs quantum dots heterostructure" Superlattices and Microstructures, Vol. 46, No. 4, pp. 611–617, October 2009 with permission from Elsevier

Figure 2.2 shows STEM images of a QD in samples 2106 and 2100, and Fig. 2.3 shows the same for samples 2109 and 2115, where the atomic structure is revealed. TEM images were taken of different portions of each of the samples; the figures show only the best images of the QDs representing the structural features of the sample. The contrast in the TEM image appears due to the difference in average atomic number of the InAs QDs and GaAs. In dark-field mode, one can expect the

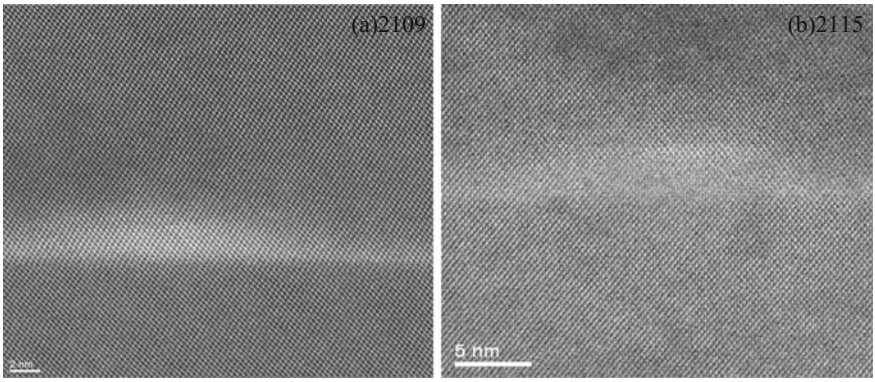

Fig. 2.3 STEM images of single QD grown at 0.197 ML/s with **a** 0 s and **b** 50 s of growth pause. Reprinted from "Investigation of effect of varying growth pauses on the structural and optical properties of InAs/GaAs quantum dots heterostructure" Superlattices and Microstructures, Vol. 46, No. 4, pp. 611–617, October 2009 with permission from Elsevier

InAs QDs will appear as brighter spot as shown in the images. The mechanism of dot formation is in accordance with the change in Gibbs free energy and the elastic relaxation energy [20].

In the STEM images, the fluctuation in contrast inside the dots arises from the inhomogeneity of In distribution within the dots. We can see from the images that in the first case, i.e. for slow growth rate, the shape of the quantum dots is trapezoidal. A compressive strain originated from the interface of the InAs QDs with the subsequent GaAs capping layer may be responsible for such trapezoidal shape.

The height and lateral size were in the range of 3–4 and 13–18 nm, respectively, for slower growth rate samples. Though the height of the dots remains almost constant, a slight increment in lateral dot size appeared as the growth pause gradually increased. Driven by epitaxial strain, some Indium-adatom migrate away from top of the QDs to the bottom, causing the increment in lateral size of samples subjected to a longer growth pause. For the faster growth rate, the QDs exhibit a shell-like structure, rather than a trapezoidal shape with larger lateral size seen in the earlier samples. The height varying from 3 to 4.5 nm with lateral size of these samples varies from 16 to 25 nm. The faster deposition rate causes quick build-up of strain energy at the bottom of the dots leading to an elongation of the lateral size. This is responsible for the shell-like appearance of the dots. The fading of the intensity at the dot apex along the interface between InAs and GaAs layers in each of the dot suggests an intermixing of In-Ga occurred.

2.2.2 Optical Characterization

The PL measurements of single-layer QD samples are shown in Figs. 2.4 and 2.5 that support the structural analysis. For both slow and fast growth-rate samples, two distinct peaks appear in the PL spectra. The lower and higher energy peaks are due to the transition from electron ground state (GS) to hole ground state and first excited electronic state to first excited ground state.

For slow growth-rate samples, distinct GS and first excited state energy peaks appear. A shift of the ground-state peak from 1.082 eV (∼1146 nm) to 1.071 eV (∼1158 nm) occurred with an increase in the duration of the growth pause. This redshift is the direct consequence of the formation of larger QDs with an increase of the growth pause [21]. The FWHM of the individual peak was measured after resolving the peaks by Gaussian function using Origin Pro-8 software. The measured FWHM of GS-emission peaks is found to vary from 30 to 40 meV. The GS energy peak and first-order excitation energy peak are not as distinct for samples with a faster growth rate. Figure 2.6 shows a shift of the ground-state peak from 1.471 eV (∼1081 nm) to 1.12 eV (∼1107 nm) when increasing the growth pause from 0 to 25 s, and then, a slight blueshift of ∼8 nm occurs with a further increase in the growth-pause duration.

Introduction of a growth pause also allows Indium out-diffusing from the core region of dots, resulting in reduced In concentration and smaller dot size. The mechanism that occurs during dot formation can be described as a competition of two counter-phenomena. Initially, larger islands are formed at the expense of the interaction between neighbouring smaller QDs [8]. Larger size tends to lower the band gap of the dots, and thus, sample 2108 exhibits redshift in the emission wavelength when compared to sample 2109. For a growth pause longer than 25 s, at higher growth rates desorption of Indium-adatom from QDs dominates the surface diffusion, causing a change in the QD morphology and hence the blueshift.

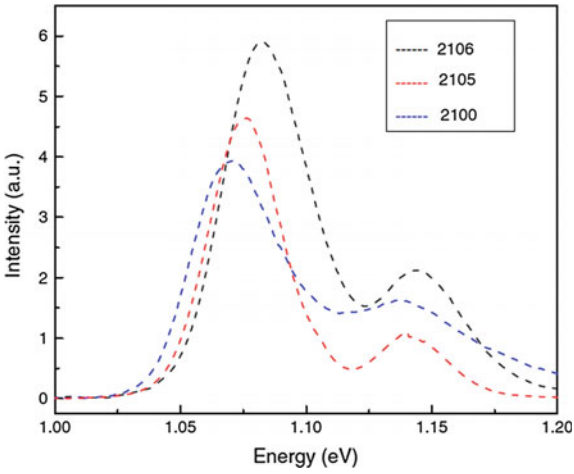

Fig. 2.4 PL-emission energies for samples 2106, 2105 and 2100 at 8 K. Reprinted from "Investigation of effect of varying growth pauses on the structural and optical properties of InAs/GaAs quantum dots heterostructure" Superlattices and Microstructures, Vol. 46, No. 4, pp. 611–617, October 2009 with permission from Elsevier

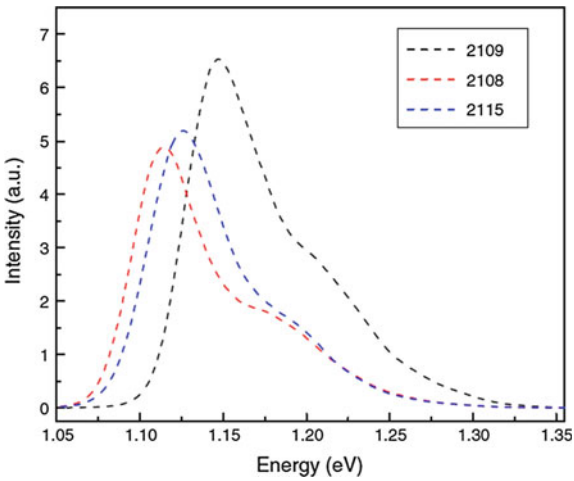

Fig. 2.5 PL-emission energies for samples 2109, 2108 and 2115 at 8 K. Reprinted from "Investigation of effect of varying growth pauses on the structural and optical properties of InAs/GaAs quantum dots heterostructure" Superlattices and Microstructures, Vol. 46, No. 4, pp. 611–617, October 2009 with permission from Elsevier

Faster growth rate induces QD size fluctuation and produces smaller dots, which causes a broadening of the linewidth of the emission peak (measured FWHM, 40–46 meV) and reduces the GS-emission wavelength. We believe that during longer growth pauses the dots have more time to interact with neighbouring dots under strained conditions and coalesce to produce larger dots which reduces dot density [22].

A similar trend appears when growing samples for device fabrication. The ground state of the PL-emission peaks for samples with 0, 25 and 50 s growth pauses (i.e. A, B and C) was observed at 1120.97, 1128.88 and 1124.78 nm, respectively, at 8 K. Thermal-activation energies calculated for each of the grown samples (A, B and C) from a typical Arrhenius plot are around 126, 117 and 89 meV for samples A, B and C, respectively, following a decreasing trend for an increase in growth-pause duration. This can be explained by the segregation of Indium from the dots towards the GaAs barrier. Intrusion of Indium-adatom in the GaAs barrier reduces the depth of the potential well, hence a gradual reduction in the activation energy. The presence of defect levels between dots and GaAs barrier during growth is another possible reason for low activation energy. Defect levels create non-radiative sites, causing degradation of sample luminescence. The existence of low activation energy for all three samples suggests the presence of non-radiative sites originating from defects and dislocations.

All three samples (A, B and C) were subjected to post-growth thermal treatment at 650, 700, 750 and 800 °C with an aim to improve the quality. Temperature-dependent PL was performed on each set of samples under identical experimental conditions, and results are compared to the as-grown sample of the same. The results are summarized in Fig. 2.6.

All three samples (A, B and C) showed significant enhancements in activation energy when annealed up to 700 °C. The thermal treatment enhanced the optical qualities by eliminating defects inside the samples. As the annealing temperature exceeded 700 °C, the thermal energy induced intermixing of InAs–GaAs, leading

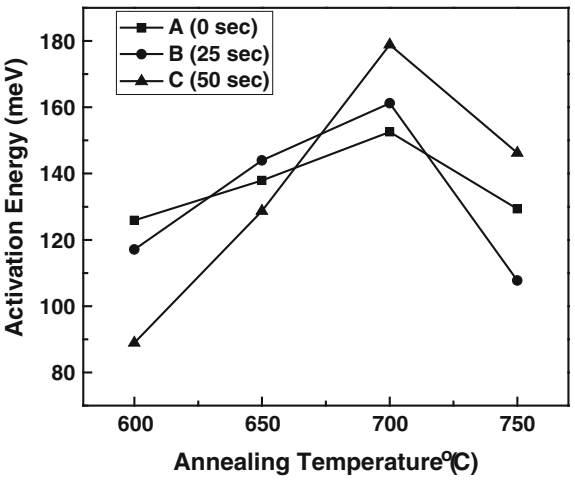

Fig. 2.6 Comparison of activation energies among the annealed counterparts of samples of all growth-pause durations

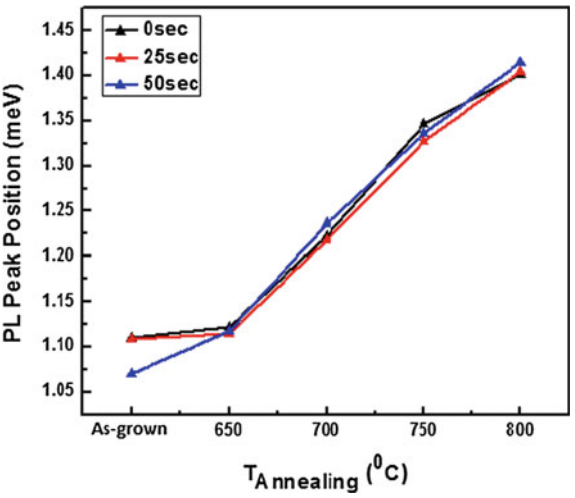

Fig. 2.7 Comparison of GS PL-emission peak of as-grown sample A, B and C and their annealed counterparts

to considerable amount of carrier escape and reducing the activation energy. The usual blueshift in the GS-emission wavelength of all three samples was observed when they were subjected to thermal annealing (Fig. 2.7).

It is evident that rapid thermal annealing causes significant change in the structural and optical properties of the as-grown heterostructure due to InAs dots–GaAs barrier intermixing. Since a particular QD heterostructure is tailored for specific uses, it is essential to develop a theoretical model to understand and predict the experimental variation in their optical properties with annealing. We have examined the experimental findings about the effect of annealing of 2106 sample with a theoretical perception in order to understand the phenomena in a better way [23]. The model was developed based on Fick's second equation.

$$\frac{\partial x(r,t)}{\partial t} = D\nabla^2 x(r,t)$$

where x denotes the mole fraction of In in $In_xGa_{1-x}As$, and D the diffusion constant of InAs is assumed to be constant throughout. We assume the as-grown QD to be composed purely of InAs and use the following initial conditions for the above equation.

$x = 1$, in the QD and WL,
$x = 0$, in the barrier material.

The equation was solved in three dimensions by discretization in both time and space, with Dirichlet boundary conditions and annealing time t = 30 s to obtain the composition of the annealed heterostructure. To explain the variation of properties with annealing temperature T_a, we consider an Arrhenius-type temperature dependence of the diffusion coefficient.

$$D = D_0 \exp\left(-\frac{E_a}{kT_a}\right)$$

where the parameters D_0 are initial diffusion coefficient and E_a = 1.23 eV, respectively.

Subsequently, the corresponding band profiles were calculated, and their variation with annealing was examined. The band profiles were used to solve for carrier energy states from the Schrödinger equation, and we observed a well-correlated blueshift in PL peak energy. Operating within a similar framework, PL spectra from the QD ensemble in the heterostructure, annealed at different temperatures, were calculated. In addition to quantitatively reproducing the variation in PL spectra, our studies shed light on changes in strain effects and potential profiles in QD materials, which may form the basis for investigations into other phenomena induced by annealing.

2.2.3 Spectral Characterization of Device

We characterized photodetector devices made of as-grown sample A and C to check the effect of growth pause on performance of the device. The normalized photocurrent of devices A and C as a function of wavelength at low temperature (50 K) at a 0.6 V operating bias is depicted in Fig. 2.8.

The photocurrent response peak ($\sim$6.0 μm) is due to the transition of carriers between QD-bound states and the quasi-bound state of the In(Ga)As wetting layer. The broadness in the linewidth of the spectrum indicates reduced confinement of the energy levels, which may be associated with the presence of defects and dislocations. The spectral response peaks of the two samples nearly coincide. Clearly,

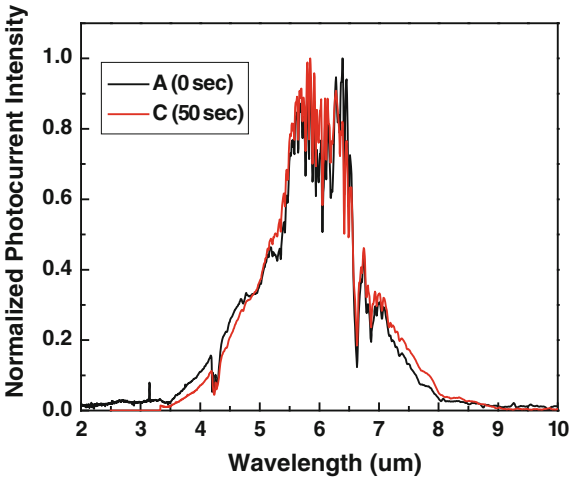

Fig. 2.8 Comparison of the spectral response results of devices A and C at 50 K

the difference in PL-emission peak is not so significant that can alter spectral response peak of the devices under consideration.

2.3 Conclusions

This study examined the effects of varying growth pauses on InAs/GaAs QD materials at two different growth rates, the effects of thermal annealing and the performance of single-pixel IR photodetector devices. The growth pause causes effective epitaxial strain to increase QD size. The optical behaviour of the samples reflects the changes in their morphology. Larger QDs decrease PL-emission energy. A small blueshift in the emission wavelength appears for samples grown at a higher growth rate and subjected to a longer ripening pause due to Indium desorption. Thus, the growth pause can serve as an important parameter in tuning the emission wavelength of InAs/GaAs QDs though the device performance may not be affected. The activation energy reduces with an increase in the duration of the growth pause due to intrusion of Indium-adatom from dots to the GaAs barrier and formation of non-radiative recombination sites that reduce the effective depth of the potential wells. Post-growth thermal treatment up to a critical limit (here 700 °C) removes these non-radiative sites and improves optical behaviour. No significant change in the spectral response of the photodetectors was observed with the introduction of growth pause.

References

1. T. Badcock, H. Liu, K. Groom, C. Jin, M. Gutierrez, M. Hopkinson et al., 1.3 μm InAs/GaAs quantum-dot laser with low-threshold current density and negative characteristic temperature above room temperature. Electro. Lett. **42**, 922–923 (2006)
2. S. Chakrabarti, A. Stiff-Roberts, P. Bhattacharya, S. Gunapala, S. Bandara, S. Rafol et al., High-temperature operation of InAs-GaAs quantum-dot infrared photodetectors with large responsivity and detectivity. IEEE Photonics Technol. Lett. **16**, 1361–1363 (2004)
3. H. Liu, S. Liew, T. Badcock, D. Mowbray, M. Skolnick, S. Ray et al., p-doped 1.3 μm InAs/GaAs quantum-dot laser with a low threshold current density and high differential efficiency. Appl. Phys. Lett. **89**, 073113 (2006)
4. D. Pan, E. Towe, S. Kennerly, A five-period normal-incidence (In, Ga) As/GaAs quantum-dot infrared photodetector. Appl. Phys. Lett. **75**, 2719–2721 (1999)
5. J. Phillips, P. Bhattacharya, S. Kennerly, D. Beekman, M. Dutta, Self-assembled InAs-GaAs quantum-dot intersubband detectors. IEEE J. Q. Electron. **35**, 936–943 (1999)
6. J. Tatebayashi, N. Hatori, H. Kakuma, H. Ebe, H. Sudo, A. Kuramata et al., Low threshold current operation of self-assembled InAs/GaAs quantum dot lasers by metal organic chemical vapour deposition. Electron. Lett. **39**, 1130–1131 (2003)
7. P. Joyce, T. Krzyzewski, G. Bell, B. Joyce, T. Jones, Composition of InAs quantum dots on GaAs (001): direct evidence for (In, Ga)As alloying. Phys. Rev. B **58**, R15981 (1998)
8. P. Joyce, T. Krzyzewski, G. Bell, T. Jones, S. Malik, D. Childs et al., Effect of growth rate on the size, composition, and optical properties of InAs/GaAs quantum dots grown by molecular-beam epitaxy. Phys. Rev. B **62**, 10891 (2000)
9. A. Convertino, L. Cerri, G. Leo, S. Viticoli, Growth interruption to tune the emission of InAs quantum dots embedded in InGaAs matrix in the long wavelength region. J. Crys. Growth **261**, 458–465 (2004)
10. D. Bhattacharyya, A. Helmy, A. Bryce, E. Avrutin, J. Marsh, Selective control of self-organized $In_{0.5}Ga_{0.5}As/GaAs$ quantum dot properties: quantum dot intermixing. J. Appl. Phys. **88**, 4619–4622 (2000)
11. J. Garcıa, G. Medeiros-Ribeiro, K. Schmidt, T. Ngo, J. Feng, A. Lorke et al., Intermixing and shape changes during the formation of InAs self-assembled quantum dots. Appl. Phys. Lett. **71**, 2014–2016 (1997)
12. A. Kosogov, P. Werner, U. Gösele, N. Ledentsov, D. Bimberg, V. Ustinov et al., Structural and optical properties of InAs–GaAs quantum dots subjected to high temperature annealing. Appl. Phys. Lett. **69**, 3072–3074 (1996)
13. J. Tatebayashi, Y. Arakawa, N. Hatori, H. Ebe, M. Sugawara, H. Sudo et al., InAs/GaAs self-assembled quantum-dot lasers grown by metalorganic chemical vapor deposition—Effects of postgrowth annealing on stacked InAs quantum dots. Appl. Phys. Lett. **85**, 1024–1026 (2004)
14. Z. Zhen, D. Bedarev, B. Volovik, N. Ledentsov, A. Lunev, M. Maksimov et al., Influence of composition and anneal conditions on the optical properties of (In, Ga) As quantum dots in an (Al, Ga) As matrix. Semiconductors **33**, 80–84 (1999)
15. Q. Zhuang, J. Li, X. Wang, Y. Zeng, Y. Wang, B. Wang et al., Effects of rapid thermal annealing on self-assembled InGaAs/GaAs quantum dots superlattice. J. Cryst. Growth **208**, 791–794 (2000)
16. R. Leon, Y. Kim, C. Jagadish, M. Gal, J. Zou, D. Cockayne, Effects of interdiffusion on the luminescence of InGaAs/GaAs quantum dots. Appl. Phys. Lett. **69**, 1888–1890 (1996)
17. S. Malik, C. Roberts, R. Murray, M. Pate, Tuning self-assembled InAs quantum dots by rapid thermal annealing. Appl. Phys. Lett. **71**, 1987–1989 (1997)
18. N. Perret, D. Morris, L. Franchomme-Fosse, R. Côté, S. Fafard, V. Aimez et al., Origin of the inhomogenous broadening and alloy intermixing in InAs/GaAs self-assembled quantum dots. Phys. Rev. B **62**, 5092 (2000)

19. C. Chia, Y. Zhang, S. Wong, S. Chua, A. Yong, S. Chow, Testing the upper limit of InAs/GaAs self-organized quantum dots density by fast growth rate. Superlattices Microstruct. **44**, 420–424 (2008)
20. U. Pohl, K. Pötschke, M. Lifshits, V. Shchukin, D. Jesson, D. Bimberg, Self-organized formation of shell-like InAs/GaAs quantum dot ensembles. Appl. Surf. Sci. **252**, 5555–5558 (2006)
21. U. Pohl, K. Pötschke, A. Schliwa, F. Guffarth, D. Bimberg, N. Zakharov et al., Evolution of a multimodal distribution of self-organized InAs/GaAs quantum dots. Phys. Rev. B **72**, 245332 (2005)
22. S. Sengupta, N. Halder, S. Chakrabarti, M. Herrera, M. Bonds, N.D. Browning, Investigation of the effect of varying growth pauses on the structural and optical properties of InAs/GaAs quantum dot heterostructures. Superlattices Microstruct. **46**, 611–617 (2009)
23. M. Srujan, K. Ghosh, S. Sengupta, S. Chakrabarti, Presentation and experimental validation of a model for the effect of thermal annealing on the photoluminescence of self-assembled InAs/GaAs quantum dots. J. Appl. Phys. **107**, 123107 (2010)

Chapter 3
Structural and Optical Characterization of Bilayer QD Heterostructures

Abstract Efforts are being made to obtain efficient quantum dot heterostructures which possess excellent uniformity in size distribution as well as capable to extend the emission wavelength to technologically useful telecommunication wavelengths, specifically 1.3 and 1.55 μm. In InAs/GaAs single-layer quantum dot (SQD) structure, higher InAs monolayer coverage for the QDs gives rise to larger dots emitting at longer wavelengths but results in inhomogeneous dot-size distribution. The bilayer quantum dots (BQDs) can be used as an alternative to SQDs, which can emit at longer wavelengths (1.229 μm at 8 K) with significantly narrow linewidth ($\sim$16.7 meV) owing vertical ordering and electronic coupling between the two layers of dots separated by a thin (7–9 nm) spacer layer. Morphological and optical properties of bilayer InAs/GaAs quantum dot heterostructure are investigated. As compared to the similar single-layer quantum dot (SQD) structure, the bilayer quantum dot (BQD) structure showed a more uniform spatial distribution and increased size homogeneity of the dots. It also exhibited longer wavelength photoluminescence (PL) emission at room temperature, with the peak at a wavelength (1.34 μm) in the infrared communication window. In an interesting study, the emission linewidth of our BQD sample is found to be insensitive towards post-growth treatments due to the strain interaction between the layers of dots.

Keywords Bilayer quantum dots · Rapid thermal annealing · Transmission electron microscope

© Springer Nature Singapore Pte Ltd. 2018

S. Sengupta and S. Chakrabarti, *Structural, Optical and Spectral Behaviour of InAs-based Quantum Dot Heterostructures*,
DOI 10.1007/978-981-10-5702-1_3

3.1 Introduction[1]

The application of InAs/GaAs self-assembled QDs in devices such as lasers and detectors is limited by size inhomogeneity of dots; this necessitates research to obtain homogeneous QDs [1, 2]. For some device applications, the vertical coupling of energy states of QDs is desirable, as it helps reduce the threshold current for injection lasing [3]. One known approach is the use of bilayer quantum dot (BQD) heterostructures [4, 5]. The BQD structure uses two closely spaced QD layers, separated by a spacer layer of the host matrix (Fig. 3.1). In a BQD system, the bottom layer (seed layer) dots provide a templating effect during the formation of the active islands in the second layer (top/active layer) due to strain coupling leading to vertically aligned QDs in the second layer. The important aspects of research into BQD systems are vertical ordering (stacking) and electronic coupling between the adjacent QD layers. Strain-driven vertical ordering of island stacks provides high-quality active QDs with uniform size distribution and large effective volume. This shifts the emissions from the active QDs to longer wavelengths with reduced emission linewidth which is an essential criterion for some telecommunication and spin-based device applications [5–9].

In last chapter, we observed that post-growth RTA can be performed to further improve the quality of dots by eliminating defects; however, post-growth thermal treatment generally results in a significant blueshift of the emission wavelength due to In/Ga intermixing and reduced dot size. Although there are some reports of improved thermal stability of coupled QDs upon annealing at 700 °C [10, 11], there has been little experimental effort in establishing a correlation between the

[1]Reprinted from, "Comparison of Luminescence Properties of Bilayer and Multilayer InAs/GaAs Quantum Dots" Materials Research Bulletin, Vol. 47, No. 1, pp. 130–134, January 2012 with permission from Elsevier.

Reprinted from, "Investigation of larger monolayer coverage in the active layer of the bilayer InAs/GaAs quantum dot structure and effects of post-growth annealing", Applied Physics A: Materials Science and Processing, Vol. 103, No. 1, pp. 245–250, April 2011 with permission from Springer.

Reprinted from, "Effect of post-growth rapid thermal annealing on bilayer InAs/GaAs quantum dot heterostructure grown with very thin spacer thickness" Materials Research Bulletin, Vol. 45, No. 11, pp. 1593–1597, November 2010 with permission from Elsevier.

Reprinted from, "Comparison of single-layer and bilayer InAs/GaAs quantum dots with a higher InAs coverage", Opto-Electronics Review, Vol. 18, No. 3, pp. 295–299, September 2010 with permission from Springer].

Reprinted from, "Vertical Ordering and Electronic Coupling in Bilayer Nanoscale InAs/GaAs Quantum Dots Separated by a Thin Spacer Layer", Nanotechnology, Vol. 19, pp. 505704, December 2008 with permission from IOP Science. © IOP Publishing. Reproduced by permission of IOP Publishing. All rights.

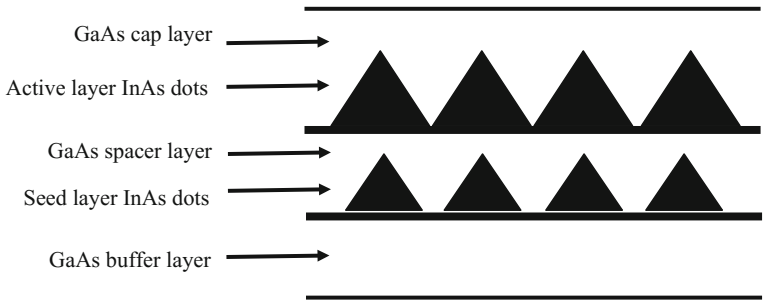

Fig. 3.1 Schematic diagram of the BQD heterostructure. Reprinted from, "Effect of post-growth rapid thermal annealing on bilayer InAs/GaAs quantum dot heterostructure grown with very thin spacer thickness" Materials Research Bulletin, Vol. 45, No. 11, pp. 1593–1597, November 2010 with permission from Elsevier

Table 3.1 Details of different InAs/GaAs BQD heterostructure samples

Sample	InAs thickness in first layer (ML)	Spacing between two layers (nm)	InAs thickness in second layer (ML)
A2044	2.5	7.5	2.5
A2046	2.5	8.5	2.5
A2047	2.5	8.5	3.2

improved thermal stability of QD stacks and vertical-strain coupling in the structures. Thermal stability is required for the growth and fabrication of certain QD-based devices, such as lasers, where the design is based on emission wavelength of the QDs.

This study investigated the effects of thin spacer thickness (7.5–8.5 nm) on the structural and luminescence properties of a BQD system and examined the effects of annealing on BQD samples and interpreted the results in terms of variations of the strain profile around active QDs due to the seed dots buried in spacer layer. The details of the samples are briefed in Table 3.1.

3.2 Results and Discussions

3.2.1 Structural Characterization

Figure 3.2 shows the Bright field cross-sectional transmission electron microscopy (BFXTM) image of the twofold nanoscale QD stack for sample (a) A2044, (b) A2046 and (c) A2047 together. It should be noted that as these TEM images were produced under bright field mode, the dots appeared as black spots surrounded by brighter portion representing the GaAs material.

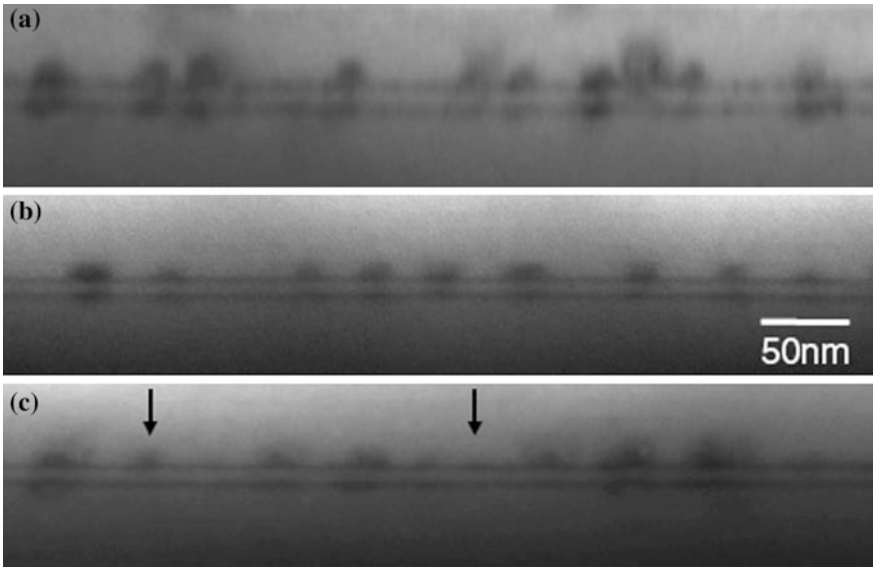

Fig. 3.2 BFXTEM images of the InAs/GaAs BQD heterostructures—**a** 2044, **b** 2046 and **c** 2047. Reprinted from, "Vertical Ordering and Electronic Coupling in Bilayer Nanoscale InAs/GaAs Quantum Dots Separated by a Thin Spacer Layer", Nanotechnology, Vol. 19, p. 505704, December 2008 with permission from IOP Science. © IOP Publishing. Reproduced by permission of IOP Publishing. All rights

The TEM micrograph reveals proper vertical ordering between the QD layers for the BQD samples (A2046 and A2047) having greater spacer thickness of 8.5 nm. While capping the InAs dots with GaAs layer, the top area of the dots effectively has a thinner GaAs layer compared to the bottom region. The deposition of GaAs tends to force the lattice constant back to that of GaAs, and the resulting buried QDs are more strained than before capping [12]. Depending upon the thickness of the spacer, the strain field can propagate to the surface of the spacer layer causing modulation of local field, thus creating preferential sites for the formation of the next dot layer, causing a self-aligned vertical coupling of the dots between two layers [13]. This strain modulation is also believed to reduce the critical thickness for 2D to 3D transitions of InAs on the top layer, resulting in the formation of bigger dots [14, 15]. In A2044 sample, the blurry contrast between the active dot layer and the GaAs material also suggests a higher degree of intermixing of material causing the formation of relatively bad quality dots. This could be due to the existence of a larger strain propagating through the narrow spacer thickness of 7.5 nm. The thickness of spacer in this sample might not be enough to cover the seed-layer dots and subsequently forming a smooth surface for the active layer dots. The 8.5-nm thickness appeared to be an optimum thickness for the growth of bilayer heterostructure under the current growth conditions. Figure 3.2c shows that some of the QDs are not coupled to the dots in the second layer (marked by arrows).

The coexistence of coupled and uncoupled islands for larger monolayer coverage in the second layer may be explained with thermodynamic equilibrium theory for lattice-mismatched systems. In a BQD system, local surface-strain minima might cause the active islands in the top layer to nucleate directly above the buried ones. A vertical correlation exists between the different QD layers. For 2.5 ML of InAs coverage, this vertical correlation is maintained exactly, but as the monolayer coverage increases, the strain increases in the non-islanded regions, leading to the formation of local uncoupled islands. The contrasts of the TEM images in both samples show that most QDs are dislocation free, which may be due to an extremely reduced growth rate for both the seed and active islands. The in situ annealing of the cap and spacer layer during the growth of the BQD structure might have an effect in the formation of dislocation-free QDs.

For the BXTEM study on the thermally annealed sample, we chosen as-grown A2046 sample and two annealed at 700 and 800 °C (this choice was made after the PL examination of the annealed samples which will be discussed in the next section). Figure 3.3 shows the BFXTEM images of the samples.

Figure 3.3a, b shows similar images of well-coupled QDs with distinct dots in the active and seed layers. The strong strain field from seed dots in the sample inhibits thermal intermixing up to 700 °C in the active layer. Careful inspection of the BFXTEM image of the sample annealed at 800 °C (Fig. 3.3c) shows that the dots in active layer have lost their shape due to material redistribution between the dots. The diminished dots in the mentioned figure prove intermixing of In/Ga as the annealing temperature reaches 800 °C. In Fig. 3.3, a small black patch appears on the top of each dot in both the active and seed layers. The dark spots are actually a strain-induced imaging defect, which often appears in high-contrast TEM imaging.

3.2.2 *Optical Characterization*

Figures 3.4 and 3.5 show the PL spectra of the bilayer structures with an Argon laser at excitation densities of 5 and 500 W/cm^2, respectively.

As seen in Table 3.1, the QDs in the top layer of sample A2047 are larger due to greater InAs monolayer coverage, compared to A2044 and A2046. This size modification effect causes a redshift in the PL-emission wavelength position for the top islands of sample A2047.

In the spectra of Fig. 3.4, the PL peak of maximum intensity arises due to electron–hole ground state (GS) transition of the top layer QDs. The FWHM for the GS peak in the PL spectrum lies between 16 and 20 meV for samples A2046 and A2047, while that of A2044 is measured $\sim$33.0 meV at 25 K. The broader PL spectra for sample A2044 are due to inhomogeneity in the active island size. This can be attributed to desorption of In from the seed dots during annealing of the thin spacer layer (S = 7.5 nm), which results in improper coupling of the strain field from the seed to the active dot layer. The spacer layer of S = 8.5 nm in the other

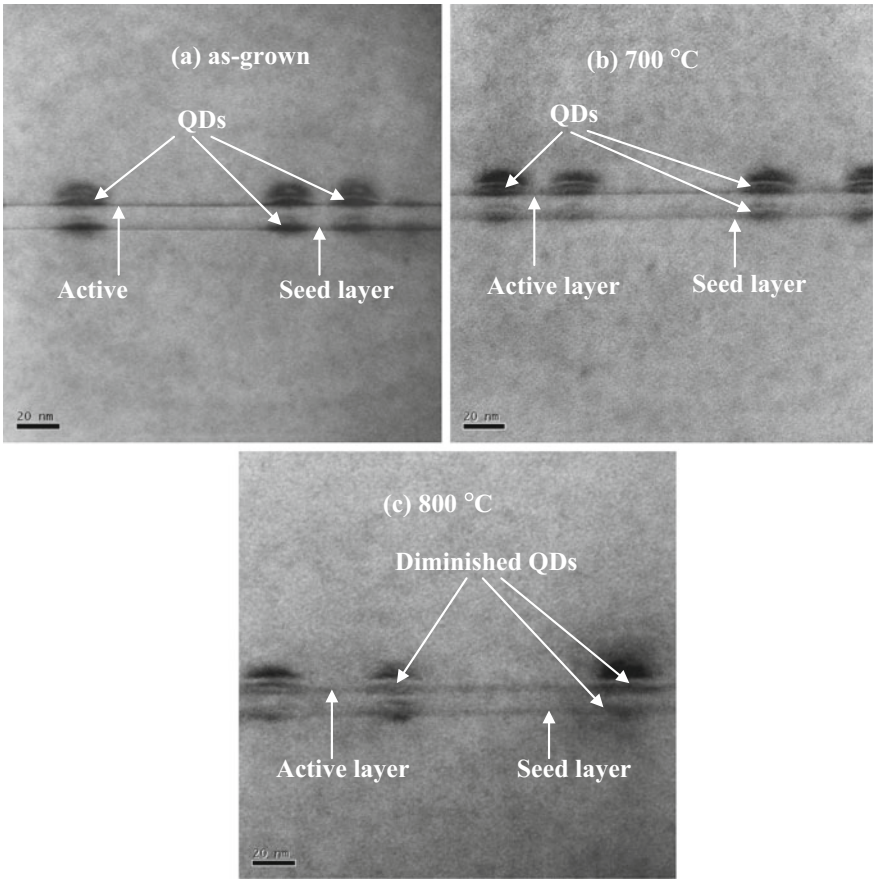

Fig. 3.3 BFXTEM images of sample A2046 **a** as-grown and annealed at **b** 700 °C and **c** 800 °C. Reprinted from, "Effect of post-growth rapid thermal annealing on bilayer InAs/GaAs quantum dot heterostructure grown with very thin spacer thickness" Materials Research Bulletin, Vol. 45, No. 11, pp. 1593–1597, November 2010 with permission from Elsevier

samples provides sufficient strain interaction from the seed dots and spacer-layer morphology to induce uniform sized dots in the second QD layer.

The multiple energy levels for the QDs in the active layer of sample (Fig. 3.5) at excitation densities of 500 W/cm^2 indicate the existence of large, defect-free active islands in the layer. The reduced In/Ga intermixing during dot capping and temperature-controlled Indium-adatom mobility resulting from the low growth temperature for the upper dots produces large coherent islands in the active layer. The peaks in the PL spectrum at 1.04, 1.09 and 1.15 eV for samples A2044 and A2046 are due to the GS, first and second excited states of electron–hole transitions for the QDs in the top layer. For sample A2047, which has comparatively greater InAs coverage (3.2 ML) in the active layer, due to an increased dot size, the peaks

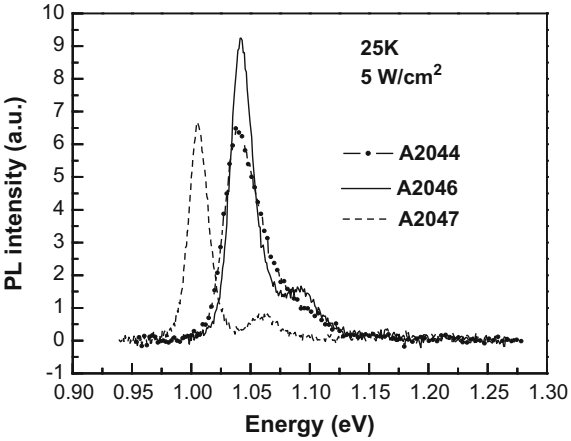

Fig. 3.4 Low-temperature (25 K) PL spectra of the three samples measured at an incident excitation power of 5 W/cm^2. Reprinted from, "Vertical Ordering and Electronic Coupling in Bilayer Nanoscale InAs/GaAs Quantum Dots Separated by a Thin Spacer Layer", Nanotechnology, Vol. 19, p. 505704, December 2008 with permission from IOP Science.© IOP Publishing. Reproduced by permission of IOP Publishing. All rights

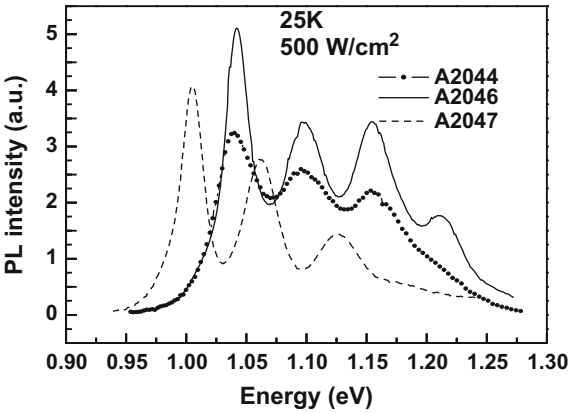

Fig. 3.5 Low-temperature (25 K) PL spectra of the three samples measured at an incident excitation power of 500 W/cm^2. Reprinted from, "Vertical Ordering and Electronic Coupling in Bilayer Nanoscale InAs/GaAs Quantum Dots Separated by a Thin Spacer Layer", Nanotechnology, Vol. 19, p. 505704, December 2008 with permission from IOP Science.© IOP Publishing. Reproduced by permission of IOP Publishing. All rights

are shifted to 1.00, 1.06 and 1.12 eV. A peak at 1.21 eV, which appears only in the PL spectra of sample A2046, can be assigned to GS emission from the seed-layer QDs. In a BQD system, the excitation transfer, i.e., the electronic tunnelling between vertically separated QD layers, depends upon the spacer thickness. For a thin spacer, the carrier-wave-function for each dot in the seed layer couples beyond

the barrier into the adjacent dots in the active layer, leading to tunnelling of the photogenerated carrier in the seed dots to the active top dots. Due to this electronic coupling, the PL spectra for the A2044 sample with a spacer thickness of 7.5 nm did not show any signal from the seed dots. Increasing the spacer thickness to 8.5 nm (in sample A2046) increased the carrier-tunnelling time to an adjacent vertically aligned dot making it greater than the recombination time leading to a signal at 1.21 eV from the seed layer (Fig. 3.5). The feeble intensity of the 1.21 eV peak in the PL spectra of sample A2046 at a high excitation density of 500 W/cm^2 signifies that a spacer thickness of 8.5 nm is not sufficient to completely quench the carrier-tunnelling effect. The surprising absence of any signal from the seed layer in the PL spectra of sample A2047, with the same spacer thickness as sample A2046 (Fig. 3.5), can only be ascribed to carriers tunnelling from the GS of the seed-layer QDs to the energy states of the top layer QDs. This tunnelling is facilitated by the larger active islands of the sample due to greater InAs monolayer coverage of the top layer, leading to enhanced quantum confinement of the carriers and much closer excited-energy states. The carriers captured in the GS of a QD in the seed layer tunnel to the excited states of the vertically aligned dots in the second layer and then rapidly relax to lower states, leading to PL emission from only the active islands for sample A2047.

The optical property of the samples was re-examined after RTA of the samples at various temperatures. This time PL experiment was done using a 532-nm He–Ne laser source. The optical properties of BQD samples attributed to annealing can be described by the balance between strain-energy modulations on the surface of the spacer layer above a buried (seed) dot and thermally driven Indium-adatom mobility/diffusivity in the active QD layer resulting from annealing. The strain energy of the active QDs plays an important role in material intermixing due to In/Ga interdiffusion. Reports in the literature suggest that the strain in regions around the InAs/GaAs QD enhances the vacancy concentration around the QD interface, which increases In/Ga interdiffusion during annealing [16–18]. The PL results of as-grown and annealed samples are plotted in same frame to compare the effects of annealing at different temperatures (Fig. 3.6). The as-grown sample contains two clearly visible peaks. The long-wavelength peak might be related to GS emissions, whereas the short-wavelength peak corresponds to transitions from the first excited state.

A close look at the short-wavelength region suggests the presence of another peak arising from transitions from the second excited state. For sample A2044, having a thin spacer (7.5 nm), the active QDs are in a larger strained state due to improper propagation of the strain field from the seed layers. It can be recalled that even at as-grown state, the dots in active layer of this sample were not well grown (see Fig. 3.2a). For sample A2044, the strained active islands assist in material diffusion during annealing even at lower annealing temperature. This accounts for the degradation of its material quality due to In/Ga intermixing and leads to a blueshift of the emission wavelength. A gradual blueshift appeared, from around 1195 to 1167 nm in the GS emission wavelength for sample A2044 due to annealing up to 700 °C (Fig. 3.6). No PL signal was detected for sample A2044

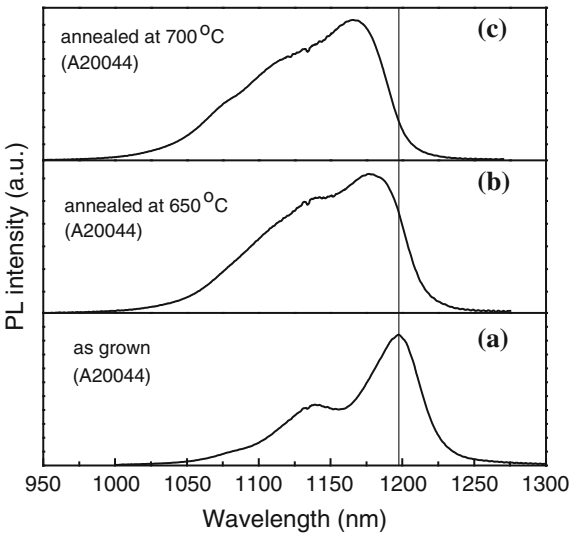

Fig. 3.6 Low-temperature (9 K) PL spectra from sample A2044, **a** as-grown and annealed at **b** 650 and **c** 700 °C. Reprinted from, "Effect of post-growth rapid thermal annealing on bilayer InAs/GaAs quantum dot heterostructure grown with very thin spacer thickness" Materials Research Bulletin, Vol. 45, No. 11, pp. 1593–1597, November 2010 with permission from Elsevier

after annealing at temperatures higher than 700 °C. This complete disappearance of the PL signal indicates thermal dissolution of dots in the wetting layer due to redistribution of material between active islands. This phenomenon is typically associated with high-temperature annealing of InAs/GaAs QDs. The increase in annealing temperature increases the lateral size of QDs before they dissolve into the wetting layer [19]. Figure 3.7 shows that the PL spectra of A2046 samples (as-grown and annealed) contain two distinct emission peaks: GS and first-excited peak. Unlike sample A2044, there is no significant shift in the GS-peak emission for samples annealed at 700 °C. The GS emission peak wavelength for the sample remains fixed at around 1185 nm after being subjected to RTA up to 700 °C. This can be attributed to the effect of spacer thickness. A2046 has thicker spacer compared to A2044 which reduces the amount of strain that propagates from seed layer to active layer dots which in turn reduces intermixing. The optimum thickness of spacer causes optimum strain propagation which is responsible for better formation of dots in the active layer. Proper propagation of strain field is capable to hold the size and shape of the dots by suppressing the usual thermal intermixing of In-Ga during the annealing till 700 °C.

Hence, the blueshift of emission wavelength peak was not observed till 700 °C annealing temperature. But thermal energy exceeds the strain field, resulting in enhanced In/Ga interdiffusion and redistribution of InAs material between islands of the active layer. This results in PL blueshift of the GS emission peak when

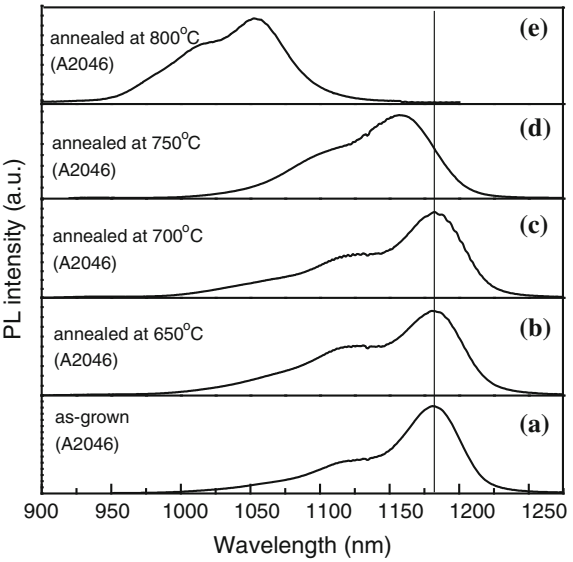

Fig. 3.7 Low-temperature (9 K) PL spectra from sample A2046, as-grown and annealed at different temperatures. Reprinted from, "Effect of post-growth rapid thermal annealing on bilayer InAs/GaAs quantum dot heterostructure grown with very thin spacer thickness" Materials Research Bulletin, Vol. 45, No. 11, pp. 1593–1597, November 2010 with permission from Elsevier

annealing beyond 700 °C (i.e., 750 °C). Increasing the annealing temperature to 800 °C shifts the GS emission peak to 1054 nm. The similar observation was recorded in case of A2047 sample as well which has same spacer thickness (i.e. 8.5 nm).

We calculated the FWHM of the GS peak for both samples A2044 and A2046 after annealing at 700 °C using a Gaussian curve fit. The variation of FWHM of the GS emission peak for as-grown and samples annealed at 700 °C is insignificant. For sample A2044, the FWHM of as-grown and annealed specimens varies between 25.0 and 27.4 meV, and from 30.2 to 32.4 eV for sample A2046. The narrow FWHM of the GS PL peak of both as-grown and annealed samples indicates nearly uniform size distribution of dots in both samples.

The results of our temperature-dependent PL study are given in Figs. 3.8 and 3.9 in the form of a typical Arrhenius plot. In all cases, the integrated PL of the GS peak is nearly constant at low temperatures, up to $\sim$100 K (not shown in the figures), which is similar to earlier reports [20]. We calculated the thermal-activation energy (E_a) corresponding to sharp PL quenching from the Arrhenius plot for sample 2046 (from Fig. 3.8). The calculated-activation energies for the as-grown and sample annealed at 700 °C are 276 and 158 meV, respectively.

We observed a drastic change in activation energy when the sample was subjected to annealing at 700 °C. Reduction of E_a with increased annealing temperature is attributed to poor confinement potential due to In/Ga interdiffusion at the dot/barrier-layer interface [21].

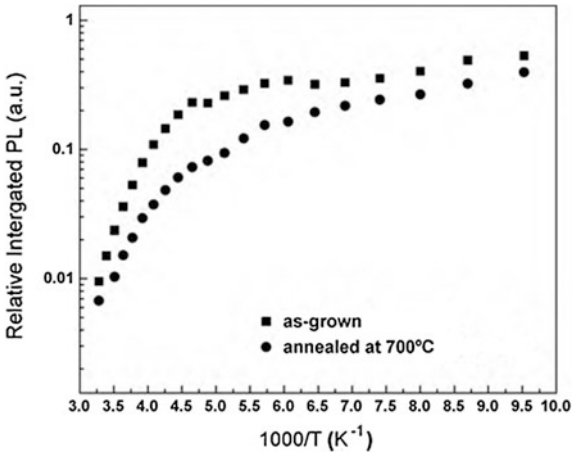

Fig. 3.8 Arrhenius plot of the temperature dependence of the integrated PL for sample A2044 both as-grown and annealed at 700 °C. Reprinted from, "Effect of post-growth rapid thermal annealing on bilayer InAs/GaAs quantum dot heterostructure grown with very thin spacer thickness" Materials Research Bulletin, Vol. 45, No. 11, pp. 1593–1597, November 2010 with permission from Elsevier

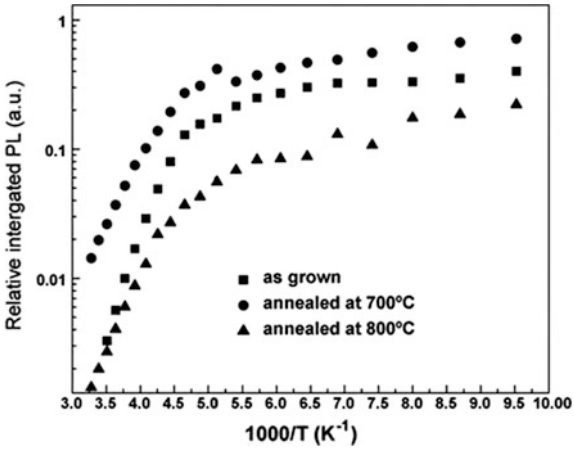

Fig. 3.9 Arrhenius plot of the temperature dependence of the integrated PL for sample A2046, as-grown and annealed at 700 and 800 °C. Reprinted from, "Effect of post-growth rapid thermal annealing on bilayer InAs/GaAs quantum dot heterostructure grown with very thin spacer thickness" Materials Research Bulletin, Vol. 45, No. 11, pp. 1593–1597, November 2010 with permission from Elsevier

For sample A2046 annealed at 700 °C, the reduction of E_a is not as drastic as for sample A2044 annealed at the same temperature (Fig. 3.9). This supports our earlier presumption that the strain-coupling effect of the seed layer maintains a stable state in QDs of the active layer of sample B, thereby minimizing In/Ga interdiffusion.

In order to provide direct evidence of our explanation, we can recall the cross-sectional TEM images of as-grown A2046 sample along with its annealed counterparts (Fig. 3.3). Figure 3.3a, b shows well-shaped distinct dots in the active and seed layers. But the image of the sample annealed at 800 °C (Fig. 3.3c) shows that the dots in active layer diminished as a result of strong intermixing of In/Ga as the annealing temperature reaches 800 °C.

3.3 Comparison of Single-Layer, Bilayer and Multilayer QD Heterostructures

3.3.1 Introduction

We compared the structural and optical properties of single QD (SQD) and bilayer QD (BQD) heterostructures. We included the characterization of a multilayer QD (MQD) heterostructure because it is a standard practise to grow number of layers of dots for fabrication of device. The QD growth mechanism of SQD samples shows that, in the SQD structure, InAs nucleation occurs randomly on the substrate. In general, InAs QDs are compressively strained due to the lattice mismatch between InAs and the GaAs substrate, which is the driving force for the self-assembled growth of InAs QDs. As we have already seen covering the QDs with a GaAs matrix introduces additional compressive strain into the buried QDs. In the case of QDs embedded in a very thin ($\sim$8.5 nm) spacer layer, the elastic-strain field along the surface of the QDs penetrates across the spacer layer. Thus, in BQD structures, there is strain modulation along the surface of the spacer layer, which acts as a growth front for the active/top QD layers, resulting in preferential growth of QDs in those areas. But growth of coupled dots in multilayer structure is subjected to precise control of different growth parameters and often results in formation of defects and dislocations which degrades the quality of the sample drastically [22–25]. In this study, we investigated the suitability of BQD heterostructure as an alternate to the conventional MQD heterostructure in terms of optical and structural properties.

3.3.2 Structural Characterization

Figure 3.10 shows the AFM images of SQD and BQD samples together. The dot densities estimated from these images are 1.5 and 1.4 $\times$ 10^{10}/cm^2, respectively. The dots in the SQD sample are not homogeneous in size and some of the dots seem clustered, making their distribution quite uneven. The dots of the BQD sample

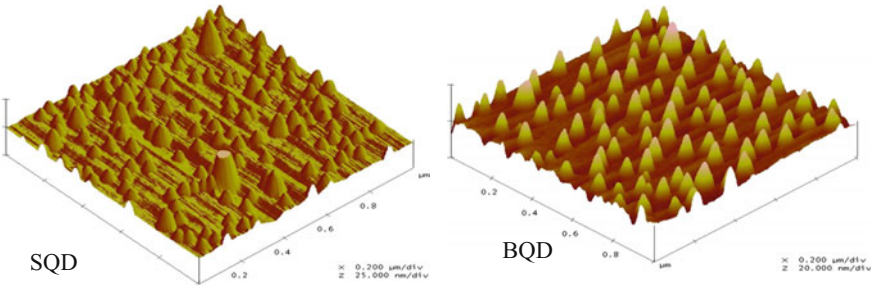

Fig. 3.10 Three-dimensional AFM images of SQD and BQD heterostructures. Reprinted from, "Comparison of single-layer and bilayer InAs/GaAs quantum dots with a higher InAs coverage", Opto-Electronics Review, Vol. 18, No. 3, pp. 295–299, September 2010 with permission from Springer

are nearly homogeneous in size and uniformly distributed on the growth front. Thus, the BQD structure with optimum spacer thickness reduces inhomogeneity in dot size resulting from higher monolayer coverage by providing a template for the growth of active (top) QDs. Figure 3.11 shows the cross-sectional TEM images of the vertically coupled MQD structures in four different areas of the same sample. The images confirm the presence of two kinds of QD stacks (the circles in the figure).

In first kind of stack (Fig. 3.11a, b), the lateral dimension of the QDs is ~20 nm. In the second kind of stack (Fig. 3.11c, d), the lateral dimension of the dots is ~25 nm. A close inspection reveals that the dot size gradually increases from the bottom layer to the top layers. The undulating nature of the growth front in the upper QD layers might be due to the accumulated strain produced due to stacking. Defects are clearly present in the stacks, which is usual in coupled structures. These defects might result from a large amount of uneven strain building during growth. Controlling the formation of defects and dislocations inside such multilayer heterostructures proves difficult, and they increase the number of non-radiative recombination sites and degrade the optical quality of the sample. This proves one of the biggest drawbacks of MQD heterostructures.

3.3.3 Optical Characterization

Figures 3.12 and 3.13 show the PL spectra of SQD and BQD samples at 8 and 300 K, respectively. At low temperature, the GS peak of the SQD sample is at 1.07 eV (1157 nm), with a linewidth of ~35.5 meV; the GS peak of the BQD sample is at 1.01 eV (1229 nm), with a linewidth of ~16.7 meV. The GS-peak wavelength of the BQD sample is significantly longer than that of the SQD sample, despite nearly identical monolayer coverage in the active dots of both samples. Figure 3.13 compares the emission wavelengths from the two samples at room

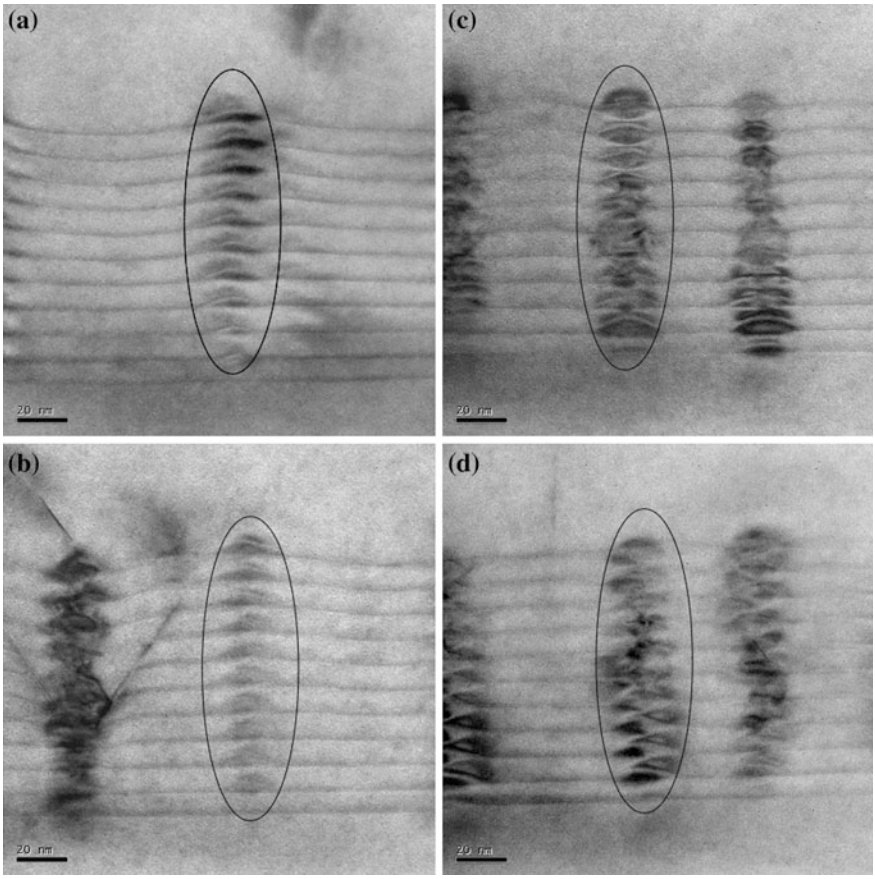

Fig. 3.11 Cross-sectional TEM images of different regions of the MQD heterostructure

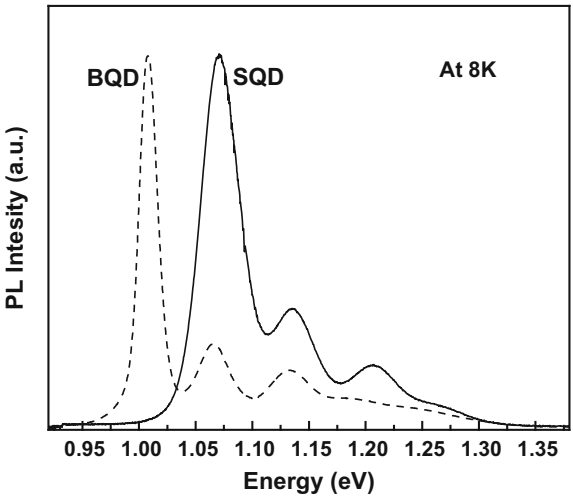

Fig. 3.12 Comparison of SQD and BQD heterostructure PL spectra at 8 K. Reprinted from, "Comparison of single-layer and bilayer InAs/GaAs quantum dots with a higher InAs coverage", Opto-Electronics Review, Vol. 18, No. 3, pp. 295–299, September 2010 with permission from Springer

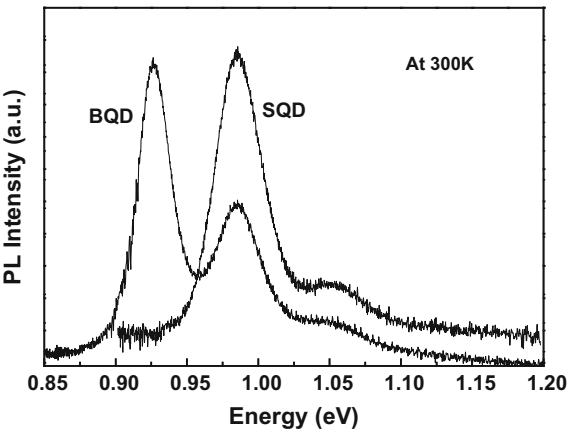

Fig. 3.13 Comparison of SQD and BQD heterostructure PL spectra at 300 K. Reprinted from, "Comparison of single-layer and bilayer InAs/GaAs quantum dots with a higher InAs coverage", Opto-Electronics Review, Vol. 18, No. 3, pp. 295–299, September 2010 with permission from Springer

temperature (300 K). The GS wavelength is at 1259 nm for the SQD structure and 1338 nm for the BQD. The non-uniform dot size in the SQD sample manifests itself in the PL spectra. Both the 8 and 300 K PL spectra show large linewidth compared to the BQD spectra. The GS PL linewidth of the SQD is nearly twice that of the BQD heterostructure, thus the BQD structure overcomes the inhomogeneity of dot size with higher monolayer coverage, by providing a template for the growth of active (top) QDs.

Additionally, the BQD heterostructure suits use in opto-electronic devices due to the significant redshift in the emission wavelength of the active dots. This is probably due to the fact that optimum spacer thickness reduces the critical thickness of dot formation in the active layer, which means the active layer dots are bigger than the same thickness SQD dots, hence redshift in emission wavelength. The BQD samples emit at 1.3 μm at room temperature, suggesting their applicability for telecommunication applications. Finally, we compare the PL-emission spectra of all three heterostructures, as shown in Fig. 3.14.

The PL spectrum of the MQD sample exhibits a particularly broad linewidth of the emission peak, with two distinct families of peaks. Both peak families persist, even at very low excitation intensities and can be attributed to the presence of two distinct sets of emitters, which may be the two different kinds of stacks discussed previously (Fig. 3.15). For InAs QDs, the peak wavelength difference between the GS and the first-excited state lies between 60 and 80 meV. The observed spectral linewidth of PL emissions for the MQD structure is due to variations in the size of the QD ensemble, referred to as inhomogeneous broadening. Carrier scattering at the strain-induced defects can also cause this broadening.

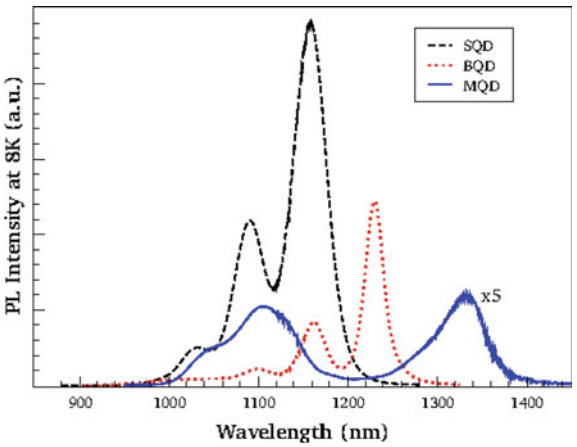

Fig. 3.14 Comparison of SQD, BQD and MQD heterostructure PL spectra at 8 K

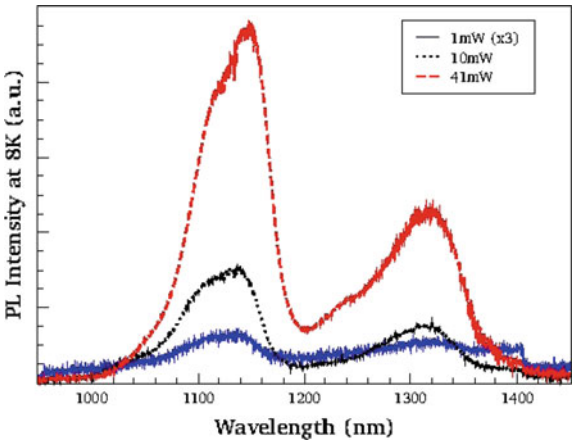

Fig. 3.15 Power-dependent PL spectra MQD heterostructure at 8 K

3.4 Conclusions

We studied the extent of vertical ordering and electronic coupling in nanoscale bilayer InAs/GaAs QD heterostructures. The spacer thickness between the seed and active layers of the BQD structure is 7.5–8.5 nm. We have found 8.5 nm spacer thickness to be the optimum spacer thickness which enables to form vertically coupled good quality dots in the active layer of the samples. We studied the effects of post-growth RTA on the same samples. As annealing temperature increased beyond 700 °C, samples with relatively less spacer thickness showed hardly any PL signal, indicating complete dissolution of the QDs. The typical blueshift of the emission peak appeared when the sample was annealed at 700 °C only due to In/Ga intermixing. For the sample with a thick spacer (8.5 nm), the emission peak does not shift significantly for annealing up to 700 °C. We presume that proper

vertical-strain coupling from seed dots reduces interdiffusion. This strain coupling maintains a stable state in the active QD layer, which prevents In/Ga interdiffusion. An insensitivity of the emission linewidth of the BQDs after annealing at 700 °C eliminates the possibility of further improvement by post-growth treatment.

The comparison of SQD, BQD and MQD samples showed that BQDs with a high (3.4 ML) InAs coverage in the active top layer exhibit optimum size uniformity, with a longer emission wavelength. The MQD heterostructure suffers from large non-uniformity of dot size and the presence of defects and dislocation in the dots further degrades the prospect of using the MQD structure for opto-electronic devices. The study suggests that repeated numbers of bilayer dots, separated by thick barrier, can be more useful for growing device samples than using the MQD heterostructures.

References

1. G. Costantini, C. Manzano, R. Songmuang, O. Schmidt, K. Kern, InAs/GaAs (001) quantum dots close to thermodynamic equilibrium. Appl. Phys. Lett. **82**, 3194–3196 (2003)
2. S. Jung, H. Yeo, I. Yun, J. Leem, I. Han, J. Kim et al., Size distribution effects on self-assembled InAs quantum dots. J. Mater. Sci. Mater. Electron. **18**, 191–194 (2007)
3. N. Ledentsov, V. Shchukin, M.E. Grundmann, N. Kirstaedter, J. Böhrer, O. Schmidt et al., Direct formation of vertically coupled quantum dots in Stranski-Krastanow growth. Phys. Rev. B **54**, 8743 (1996)
4. Y.I. Mazur, Z.M. Wang, G. Tarasov, M. Xiao, G. Salamo, J. Tomm et al., Interdot carrier transfer in asymmetric bilayer InAs/GaAs quantum dot structures. Appl. Phys. Lett. **86**, 063102–063102-3 (2005)
5. P. Howe, B. Abbey, E. Le Ru, R. Murray, T. Jones, Strain-interactions between InAs/GaAs quantum dot layers. Thin Solid Films **464**, 225–228 (2004)
6. A. Hospodkova, E. Hulicius, J. Oswald, J. Pangrác, T. Mates, K. Kuldová et al., Properties of MOVPE InAs/GaAs quantum dots overgrown by InGaAs. J. Cryst. Growth **298**, 582–585 (2007)
7. K. Nishi, H. Saito, S. Sugou, J.-S. Lee, A narrow photoluminescence linewidth of 21 meV at 1.35 μm from strain-reduced InAs quantum dots covered by In 0.2 Ga 0.8 As grown on GaAs substrates. Appl. Phys. Lett. **74**, 1111–1113 (1999)
8. M. Usman, S. Heck, E. Clarke, P. Spencer, H. Ryu, R. Murray et al., Experimental and theoretical study of polarization-dependent optical transitions in InAs quantum dots at telecommunication-wavelengths (1300-1500 nm). J. Appl. Phys. **109**, 104510 (2011)
9. M. Taylor, P. Spencer, E. Clarke, E. Harbord, R. Murray, Tuning exciton g-factors in InAs/GaAs quantum dots. J. Phys. D Appl. Phys. **46**, 505105 (2013)
10. N. Jin-Phillipp, K. Du, F. Phillipp, M. Zundel, K. Eberl, Thermal stability of stacked self-assembled InP quantum dots in GaInP. J. Appl. Phys. **91**, 3255–3260 (2002)
11. A. Zhukov, A.Y. Egorov, A. Kovsh, V. Ustinov, N. Ledentsov, M. Maksimov et al., Injection heterolaser based on an array of vertically aligned InGaAs quantum dots in a AlGaAs matrix. Semiconductors **31**, 411–414 (1997)
12. P. Joyce, E. Le Ru, T. Krzyzewski, G. Bell, R. Murray, T. Jones, Optical properties of bilayer InAs/GaAs quantum dot structures: influence of strain and surface morphology. Phys. Rev. B **66**, 075316 (2002)
13. E. Clarke, P. Spencer, E. Harbord, P. Howe, R. Murray, Growth, optical properties and device characterisation of InAs/GaAs quantum dot bilayers. J. Phys. Conf. Ser. 012003 (2008)

14. C. Priester, Modified two-dimensional to three-dimensional growth transition process in multistacked self-organized quantum dots. Phys. Rev. B **63**, 153303 (2001)
15. Q. Xie, A. Madhukar, P. Chen, N.P. Kobayashi, Vertically self-organized InAs quantum box islands on GaAs (100). Phys. Rev. Lett. **75**, 2542 (1995)
16. J. Johansson, W. Seifert, V. Zwiller, T. Junno, L. Samuelson, Size reduction of self assembled quantum dots by annealing. Appl. Surf. Sci. **134**, 47–52 (1998)
17. S.W. Ryu, I. Kim, B.D. Choe, W.G. Jeong, The effect of strain on the interdiffusion in InGaAs/GaAs quantum wells. Appl. Phys. Lett. **67**, 1417–1419 (1995)
18. L. Selen, L. Van IJzendoorn, M. de Voigt, P. Koenraad, Evidence for strain in and around InAs quantum dots in GaAs from ion-channeling experiments. Phys. Rev. B **61**, 8270 (2000)
19. A. Babiński, J. Jasiński, R. Bożek, A. Szepielow, J. Baranowski, Rapid thermal annealing of InAs/GaAs quantum dots under a GaAs proximity cap. Appl. Phys. Lett. **79**, 2576–2578 (2001)
20. R. Heitz, I. Mukhametzhanov, A. Madhukar, A. Hoffmann, D. Bimberg, Temperature dependent optical properties of self-organized InAs/GaAs quantum dots. J. Electron. Mater. **28**, 520–527 (1999)
21. C.M. Lee, S.K. Noh, J.I. Lee, D.-H. Lee, J.-Y. Leem, I.K. Han et al., Optical properties of In0. 5Ga0. 5As/GaAs quantum dots grown by heterogeneous droplet epitaxy with post-growth annealing. J. Korean Phys. Soc. **41**, L579–L582 (2002)
22. J. Ng, U. Bangert, M. Missous, Formation and role of defects in stacked large binary InAs/GaAs quantum dot structures. Semicond. Sci. Technol. **22**, 80 (2007)
23. J. Yang, P. Bhattacharya, Z. Mi, High-performance In 0.5 Ga 0.5 As/GaAs quantum-dot lasers on silicon with multiple-layer quantum-dot dislocation filters. IEEE Trans. Electron Devices **54**, 2849–2855 (2007)
24. J. Suseendran, N. Halder, S. Chakrabarti, T. Mishima, C. Stanley, Stacking of multilayer InAs quantum dots with combination capping of InAlGaAs and high temperature grown GaAs. Superlattices Microstruct. **46**, 900–906 (2009)
25. S. Adhikary, N. Halder, S. Chakrabarti, S. Majumdar, S. Ray, M. Herrera et al., Investigation of strain in self-assembled multilayer InAs/GaAs quantum dot heterostructures. J. Cryst. Growth **312**, 724–729 (2010)

Chapter 4
Optical and Spectral Characterization of Sub-monolayer QDIPs

Abstract In this chapter, we have explored the properties of an unconventional type of quantum dots, namely sub-monolayer (SML) quantum. We have performed a systematic study to optimize different growth parameters and have investigated structural and optical properties of the materials. We have successfully demonstrated high device performance of sub-monolayer quantum dots infrared photodetector with confinement-enhancing (CE) barrier and compared with conventional Stranski–Krastanov quantum dots with a similar design. This quantum-dots-in-a-well structure with CE barrier enables higher quantum confinement and increased absorption efficiency due to stronger overlap of wave-functions between the ground state and the excited state. Normal incidence photoresponse peak is obtained at 7.5 μm with a detectivity of 1.2×10^{11} cm $Hz^{1/2}$ W^{-1} and responsivity of 0.5 A/W (77 K, 0.4 V, *f*/2 optics). Using photoluminescence and spectral-response measurements, the band structure of the samples was deduced semi-empirically.

Keywords Sub-monolayer quantum dots · Confinement-enhancing barrier · Photodetectors

4.1 Introduction[1]

Several groups have demonstrated dramatic improvements in QDIPs grown with the S–K mode by introducing different material compositions and novel architectures, such as resonant tunnelling QDIPs, superlattice-based QDIPs,

[1]Reprinted from, "A comprehensive study on molecular beam epitaxy-grown InAs sub-monolayer quantum dots with different capping combinations", J. Vac. Sci. Technol. B 31(3), 03C136-1, May/Jun 2013 with permission from AIP publishing LLC.

Reprinted from, "Multi-stack InAs/InGaAs sub-monolayer Quantum Dots Infrared Photodetectors", Applied Physics Letters, Vol. 102, p. 011131, 2013 with permission from AIP publishing LLC.

Reprinted from S. Sengupta et al., "Sub-monolayer quantum dots in confinement enhanced dots-in-a-well heterostructure," Applied Physics Letters, Vol. 100, p. 191111, 2012 with permission from AIP publishing LLC.

© Springer Nature Singapore Pte Ltd. 2018

S. Sengupta and S. Chakrabarti, *Structural, Optical and Spectral Behaviour of InAs-based Quantum Dot Heterostructures*,
DOI 10.1007/978-981-10-5702-1_4

quantum-dots-in-a-well (DWELL), quantum-dots-in-a-double-well (DDWELL), InAlGaAs-capped QDs and successfully demonstrated high-performance devices [1–12]. A typical DWELL structure, where InAs quantum dots are confined inside a InGaAs-GaAs quantum well (QW), allows tuning of the detection-peak wavelength, while providing lower dark current and higher operating temperature [13, 14]. Introducing confinement-enhancing (CE) barriers surrounding the dots increases the absorption quantum efficiency (QE) and confinement of electron wave-function. *Barve et al.* suggested an architecture that employs 2-nm-thick $Al_{0.22}Ga_{0.78}$ CE barriers around the DWELL structure [15]. Such blocking layers in the transport direction reduce the dark current significantly while enhancing the absorption coefficient and increasing the escape probability. Even after devoting constant effort to improve the performance of S–K quantum-based optoelectronics devices, it could not meet the predicted expectation. The fluctuation in the size uniformity of dots, low effective area and presence of wetting layer are regarded as the biggest disadvantages of the S–K growth mode. While a considerable effort has been made to improve the barrier design and composition, few studies have gone beyond the idea of S–K-mode QDs.

Due to the nature of formation, wetting layer - a 2D QW-like structure is always present with S-K mode dots (Fig. 4.1). Although QD theory suggests complete carrier confinement, using the S–K growth mode can only obtain heterostructures that provide a mixture of 2D and 3D confinement. The presence of a wetting layer reduces the degree of carrier confinement and does not contribute to the normal incidence absorption. The non-uniform distribution of dots broadens the emission linewidth which restricts the improvement of the optoelectronics device performance. Sub-monolayer (SML) QD-based design appears to be a promising solution [16–19]. The SML QD structure is typically grown by depositing a fraction of a monolayer of QD material (InAs or InGaAs) on the host matrix. Then, a very thin (typically from a few angstroms to nanometres) spacer layer (GaAs/InGaAs/InAlGaAs or suitable combinations of these materials) is deposited before the next deposition of InAs sub-monolayer as shown in (Fig. 4.2).

This avoids the formation of any wetting layer, resulting in better quantum confinement and increased carrier wave-function overlap. Depending upon the thickness of the spacer inserted between consecutive repetitions of InAs depositions (referred to as a stack), the layers may or may not be vertically correlated to each

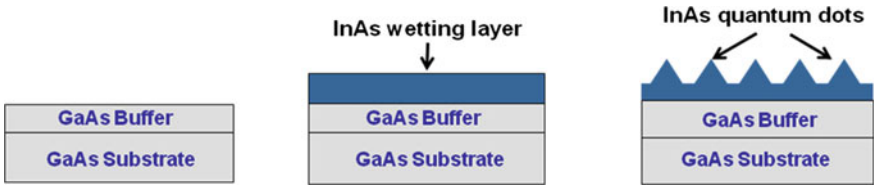

Fig. 4.1 Schematic of the S–K growth mechanism

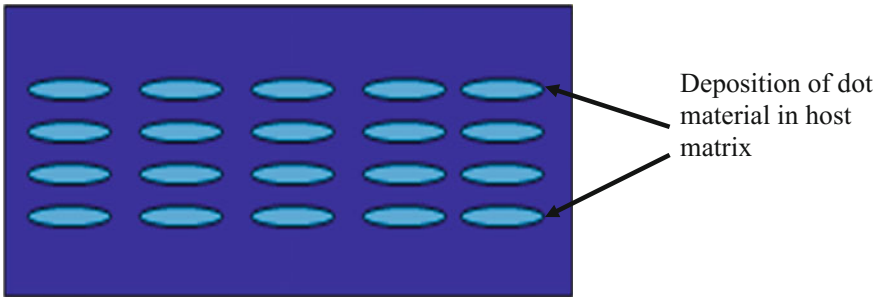

Fig. 4.2 Schematic design of the SML growth mode

other. The number of stacks can vary and is subjected to the precise optimization in order to achieve best result. SML QDs provide high dot density due to smaller (∼5 nm) lateral size and narrow average lateral spacing (∼2 nm) between dots, leading to higher absorption efficiency [20, 21]. Though the idea of SML dots is simple, the realization of the same in practice demands accurate control over the growth parameters. It is difficult to observe SML dots even through the best of electronic microscope imaging technique due to the extremely small feature size. There are very few reports available on the structural evidence of formation of such dots in the literature [21–24]. But high optical quality makes SML dots an attractive option for optoelectronics device application. A number of citations on the high performance of SML dots-based lasers and diodes are available in the literature [24–27]. Surprisingly not much work has been reported on SML growth-mode-based QDIPs despite being very eligible candidate for the same [28].

The work on SML photodetectors is divided into two parts. First, we carried out the groundwork to optimize the important parameters, such as the number of InAs stacks, the thickness and material combinations of the spacer [29]. Then, we demonstrated high-performance SML QDIP devices and compared them to S–K QDIP devices [30, 31].

4.2 Optimization of the SML Heterostructure

We compiled a comprehensive study of sub-monolayer InAs QDs with different spacer/capping layers. This work is divided into two distinct parts. First, we optimized the thickness of InAs deposition and GaAs spacer. All samples were grown without contact layers and were characterized only by low-temperature PL spectra. We then examined the effects of different capping combinations on the SML dots. Three samples (A, B and C) were grown and characterized with temperature-dependent PL. Finally, we fabricated single-pixel photodetector devices using samples A, B and C and performed device characterization.

4.2.1 Results and Discussions

4.2.1.1 Optical Characterization

A PL comparison (at 8 K) of the PL samples with varying InAs sub-monolayer depositions is presented in Fig. 4.3. We varied the thickness of the InAs material from 0.3 to 0.8 ML; each sample had four InAs/GaAs deposition stacks. The peak wavelength due to the GS transition of carriers inside the dots shifts towards a higher wavelength with increased InAs material deposition.

This redshift occurred at approximately 837–874 nm. As InAs deposition increases, dot size increases and the redshift is observed.

The narrow FWHM value suggests higher dot uniformity. Since all of our samples showed similar luminescence properties, we chose 0.5 ML as our optimized thickness. A PL comparison of the samples with varying GaAs capping thicknesses is shown in Fig. 4.4. We maintained identical growth conditions and used three different capping thicknesses: 1.5, 2.0 and 2.5 nm. A redshift appeared from 844 to 853 nm with increasing well thickness. As all samples had similar luminescence, we chose 2 nm as the optimized capping thickness.

As described earlier, we grew and characterized three device samples with fixed 4-stack 0.5-ML InAs deposition, using different capping combinations but keeping the total thickness same (2.0 nm). PL experiments at room temperature (Fig. 4.5) show a GS-emission peak from the dots at 898, 917 and 867 nm for samples A, B and C, respectively. This high-energy band gap for InAs dots is due to their small

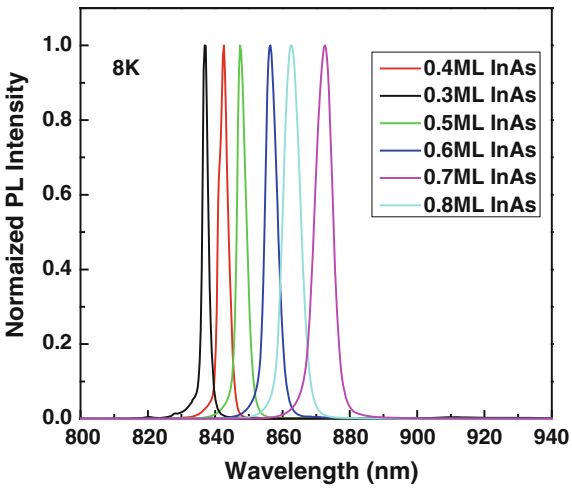

Fig. 4.3 Low-temperature (8 K) PL spectra of samples with varying InAs thickness. Reprinted from, "A comprehensive study on molecular beam epitaxy-grown InAs sub-monolayer quantum dots with different capping combinations", J. Vac. Sci. Technol. B 31(3), 03C136-1, May/Jun 2013 with permission from AIP publishing LLC

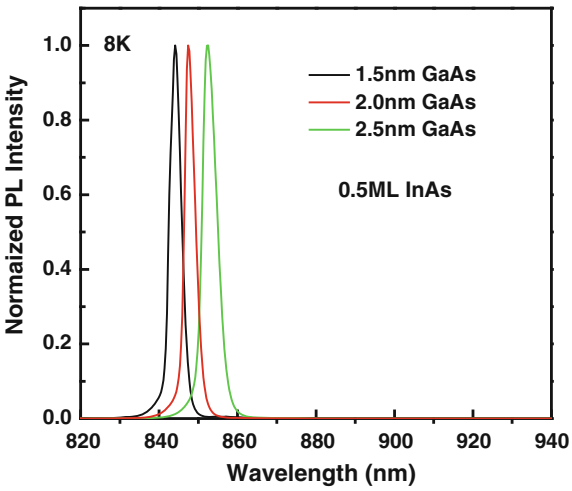

Fig. 4.4 Low-temperature (8 K) PL spectra with varying GaAs barrier thickness. Reprinted from, "A comprehensive study on molecular beam epitaxy-grown InAs sub-monolayer quantum dots with different capping combinations", J. Vac. Sci. Technol. B 31(3), 03C136-1, May/Jun 2013 with permission from AIP publishing LLC

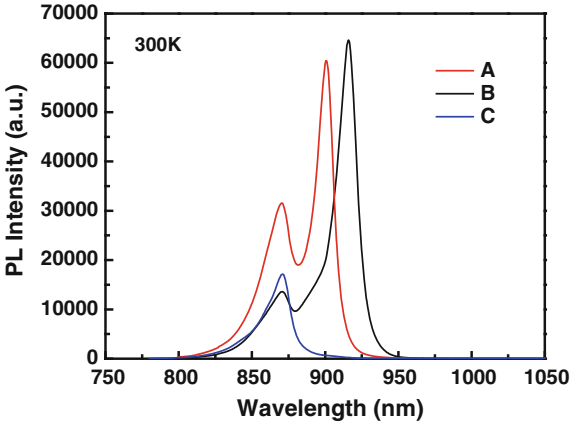

Fig. 4.5 Room-temperature PL spectra of samples A, B and C. Reprinted from, "A comprehensive study on molecular beam epitaxy-grown InAs sub-monolayer quantum dots with different capping combinations", J. Vac. Sci. Technol. B 31(3), 03C136-1, May/Jun 2013 with permission from AIP publishing LLC

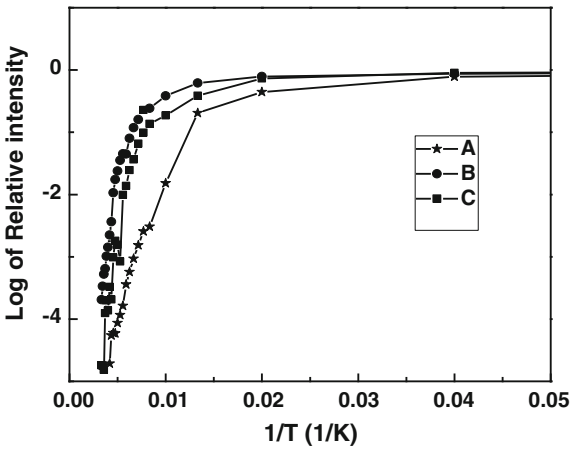

Fig. 4.6 Arrhenius plot from temperature-dependent PL experiments. Reprinted from, "A comprehensive study on molecular beam epitaxy-grown InAs sub-monolayer quantum dots with different capping combinations", J. Vac. Sci. Technol. B 31(3), 03C136-1, May/Jun 2013 with permission from AIP publishing LLC

size. For sample C, the wavelength shift towards a lower value is probably due to Al migration into the dots from the capping layer. The FWHM remains in the range of 19–32 meV at 300 K, indicating high uniformity of the dot-size distribution.

We investigated the change in carrier confinement of the different samples by measuring the temperature-dependent PL quenching using the conventional Arrhenius plot. We calculated the thermal-activation energies for A, B and C as 49, 112 and 109 meV, respectively (Fig. 4.6). The lower activation energy of sample A is attributed to the higher degree of InAs-GaAs intermixing. In samples B and C, the capping material contained amounts of In to compensate for the In out-diffusion from the dot cores, hence the reduction in intermixing.

4.2.1.2 Spectral Characterization of Device

Next, we characterized single-pixel photodetectors fabricated from samples A, B and C. We measured the I-V of all of the devices at 77 K to obtain the dark-current density (Fig. 4.7). The dark current was calculated in the range of 10^{-5} to 10^{-4} A/cm^2 at a 0.5 V applied bias at 77 K, which is higher than the usual dark current for such devices.

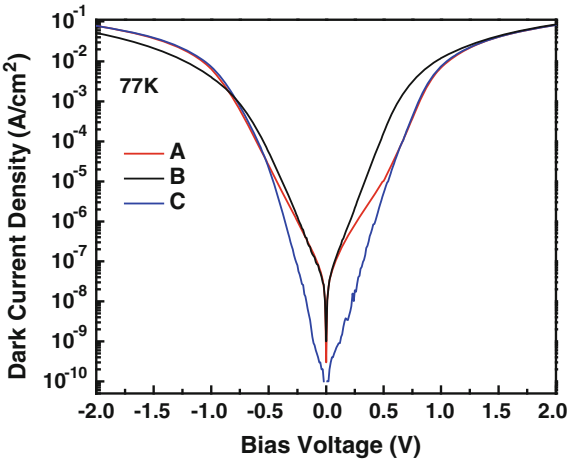

Fig. 4.7 Dark-current variation of devices A, B and C as a function of the applied bias voltage at 77 K. Reprinted from, "A comprehensive study on molecular beam epitaxy-grown InAs sub-monolayer quantum dots with different capping combinations", J. Vac. Sci. Technol. B 31 (3), 03C136-1, May/Jun 2013 with permission from AIP publishing LLC

4.3 Demonstration of High-Performance SML QDIPs

We chose a different design for the fabrication of SML QDIPs. We implemented the concept of a CE barrier with DWELL architecture, originally proposed for S–K QDIP devices. Initially, we grew a number of device samples with a varying number of InAs stacks and examined their optical and spectral properties including spectral-response spectra and detectivity measurements. We compared the best device from this lot to an S–K QDIP device with an equivalent architecture.

4.3.1 Results and Discussions

4.3.1.1 Optical Characterization

Figure 4.8 depicts the normalized PL spectra obtained from the SML device samples with a varying number of stacks, where each stack has 0.3 ML of InAs deposition. The GS-emission energy decreases from 1.32 to 1.26 eV with an increased number of stacks. The redshift in the emission wavelength for an increased number of stacks is due to enhancement in the effective dot volume. The FWHM of the emission peaks remains in the range of 33–48 meV.

The PL spectra showed no evidence of excited states inside the dots despite the use of a high-power excitation laser. The dots are too small to accommodate any

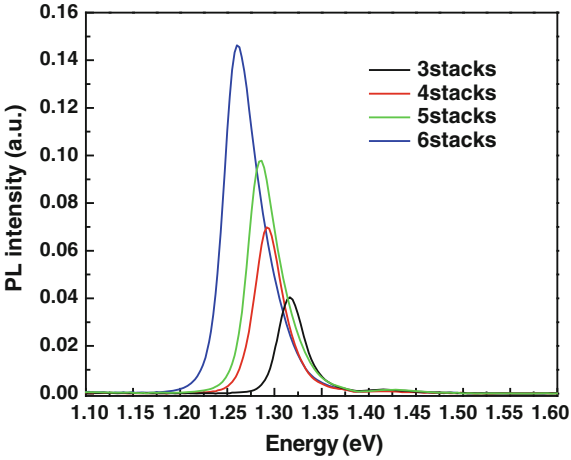

Fig. 4.8 PL spectra of device samples with a varying number of stacks at room temperature

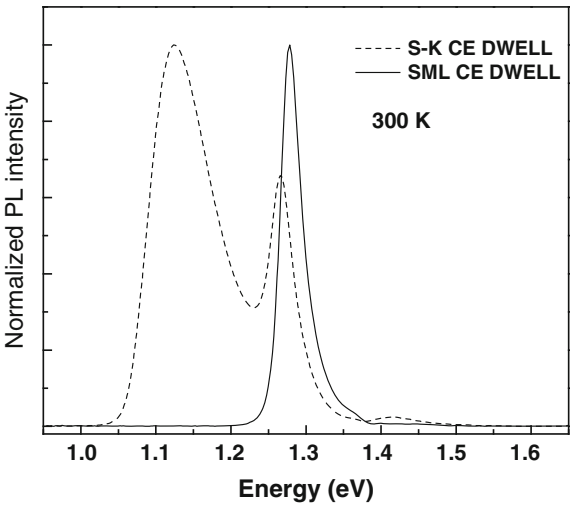

Fig. 4.9 Comparison of the PL for S–K- and SML-mode samples at room temperature. Reprinted from S. Sengupta et al., "Sub-monolayer quantum dots in confinement enhanced dots-in-a-well heterostructure", Applied Physics Letters, Vol. 100, p. 191111, 2012 with permission from AIP publishing LLC

excited state. The samples showed no significant difference in luminescence efficiency.

Figure 4.9 shows the PL spectra of a 4-stack SML device sample (we choose this sample for our comparison as it exhibited the best device performance) and that of S–K QDIP sample. The GS-emission peak is at 1.12 eV for the S–K sample and 1.28 eV for the SML. The blueshift that appears in the GS PL peak might arise due to the smaller size of SML QDs compared to the S–K QDs. The narrower FWHM of the PL spectrum for SML QDs ($\sim$35 meV) suggests high uniformity of the size distribution.

Power-dependent PL experiments confirmed the existence of the first excited state in S–K QDs—it appears at 1.27 eV. It should be noted that the GS-emission peak of SML QDs coincides with the first excited emission peak of the S–K QDs.

4.3.1.2 Spectral Characterization

Figure 4.10 compares the data for normal incidence, spectral response measured for four SML QDIPs, with the number of stacks varied from 3 to 6. It exhibited a peak at ~7.5 μm due to transitions between the GS of the SML QDs and the excited state of the QW.

The spectral response of devices consisting of 3 stacks of SML QDs is broader as compared to the other devices. The 8.4-μm peak present in the 3-stack device is not completely blocked by the CE barrier.

Radiometric measurements, using a blackbody source calibrated at 900 K, measured the detectivity (D^*) and responsivity (R) of the devices at 77 K. The highest D^* value measured was 1.2×10^{11} cm $Hz^{1/2}$ W^{-1} (at 77 K, 0.4 V, 7.5 μm, $f/2$ optics) for the 4-stack SML QDIP device (Fig. 4.11). D^* increases with an increase in the number of stacks up to four and then decreases with more stacks. The dark current in 3-stack devices proved higher than that for devices with 4–6 stacks.

The responsivities of devices with 3–6 stacks were ~0.08, ~0.45, ~0.3 and ~0.1 A/W, respectively. Again the 4-stack sample outperformed the other samples, making 4 the optimum number of stacks for such devices.

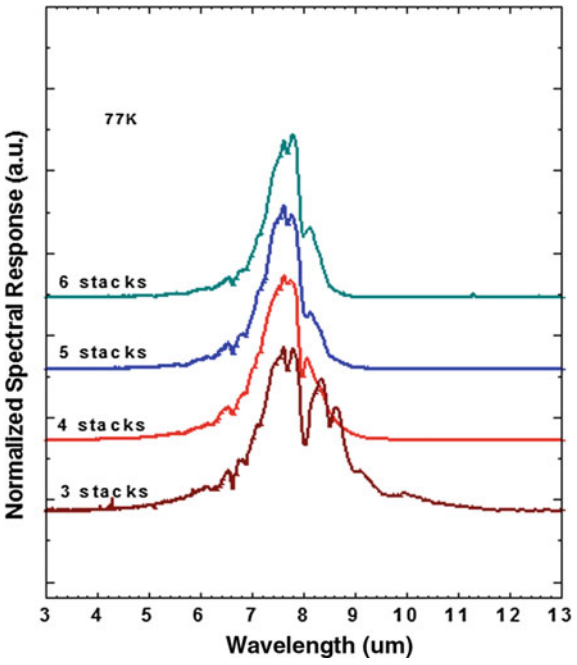

Fig. 4.10 Comparison of normalized photocurrent spectra of QDIP devices with a varying number of stacks at 77 K. Reprinted from, "Multi-stack InAs/InGaAs sub-monolayer Quantum Dots Infrared Photodetectors", Applied Physics Letters, Vol. 102, p. 011131, 2013 with permission from AIP publishing LLC

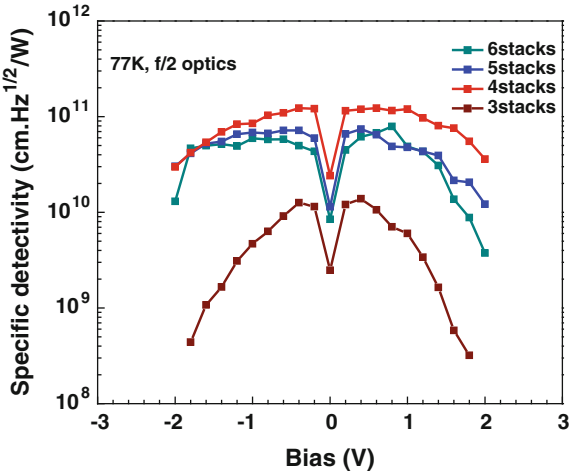

Fig. 4.11 Detectivity as a function of the applied bias voltage for QDIP devices with a varying number of stacks at 77 K. Reprinted from, "Multi-stack InAs/InGaAs sub-monolayer Quantum Dots Infrared Photodetectors", Applied Physics Letters, Vol. 102, p. 011131, 2013 with permission from AIP publishing LLC

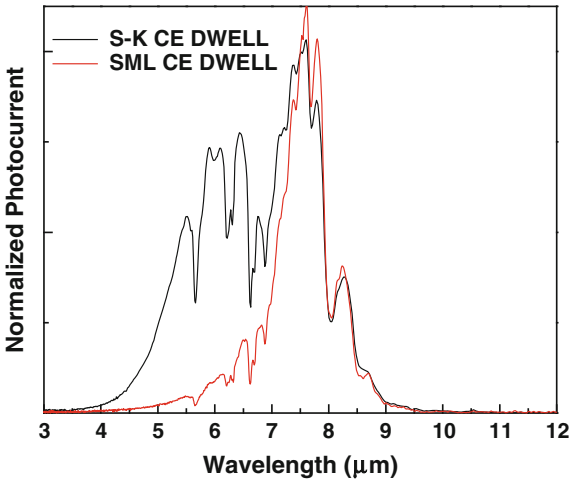

Fig. 4.12 Comparison of the normalized photocurrents of S–K and SML QDIPs at 77 K. Reprinted from S. Sengupta et al., "Sub-monolayer quantum dots in confinement enhanced dots-in-a-well heterostructure", Applied Physics Letters, Vol. 100, p. 191111, 2012 with permission from AIP publishing LLC

We compared the 4-stack SML device to an S–K QDIP device with a similar architecture. Figure 4.12 shows the comparison of the spectral responses.

While the photocurrent response from the S–K QD shows main peaks at 6.5 and 7.5 μm, the SML QD sample shows response only at 7.5 μm. A detailed analysis of

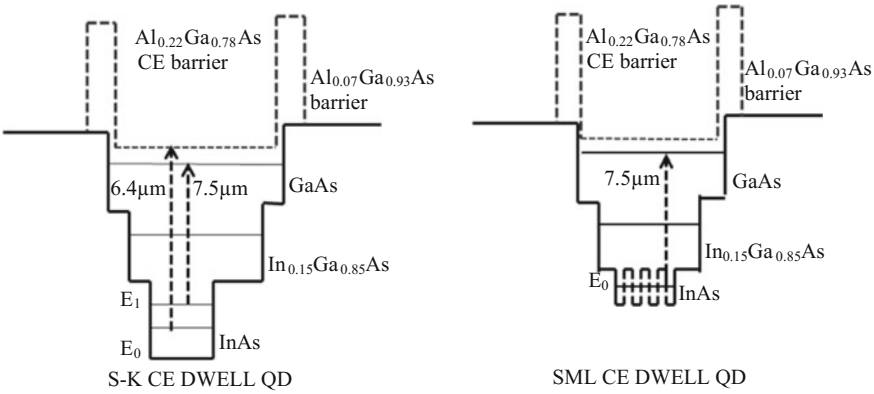

Fig. 4.13 Comparison of S–K- and SML-mode band structures. Reprinted from S. Sengupta et al., "Sub-monolayer quantum dots in confinement enhanced dots-in-a-well heterostructure", Applied Physics Letters, Vol. 100, p. 191111, 2012 with permission from AIP publishing LLC

S–K dots in CE DWELL is reported here. The photocurrent peak of the SML QD appears symmetric for both polarities of applied bias voltage. The peak at 7.5 μm for the S–K QD is identified as the transition between the excited state of the QD (E_1) and the excited state in the QW. The origin of the 7.5-μm peak in the SML QD is the transition between the GS of the QD (E_0) and the excited state in the QW. The appearance of a photocurrent response peak at 7.5 μm for both samples supports our conclusions from PL measurements. Combining the information from PL experiments and spectral-response measurements, we semi-empirically reconstructed the band structures of the heterostructures, as shown in Fig. 4.13.

Figure 4.14 compares the dark-current density of SML and S–K QDIPs at 77 K. Because of employment of current blocking and the CE barrier in the transport direction, both device types produce low dark current [15].

Figures 4.15 and 4.16 show the comparison of specific detectivity (D^*) and peak responsivity (R) between S–K and SML QDIPs.

The highest D^* for SML QD is 1.2×10^{11} cm $Hz^{1/2}/W$ at a bias of 0.4 V. The D^* for the SML QD is almost double that for the S–K QD device. Figure 4.16 shows a significant improvement of R over the whole bias range. As the detection peak is due to the transition between bound state in QD and excited energy in the QW, which is close to the continuum energy level, the escape probability of photocarriers is higher. This results a low operational bias and high responsivity which in turn increases the detectivity value. High responsivity also indicates high absorption quantum efficiency (QE). The low operating bias voltage makes the SML feasible for fabrication of FPAs using commercially available silicon read-out circuits.

To understand the transport mechanism inside the SML QD device, we measured the photoconductive gain and estimated the absorption QE of SML QD device. The PC gain was calculated using the following equation:

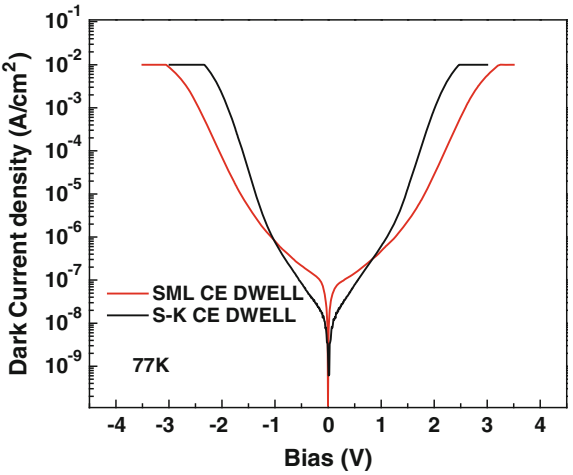

Fig. 4.14 Dark current as a function of the applied bias voltage of QDIPs grown by S–K and SML growth modes, measured at 77 K

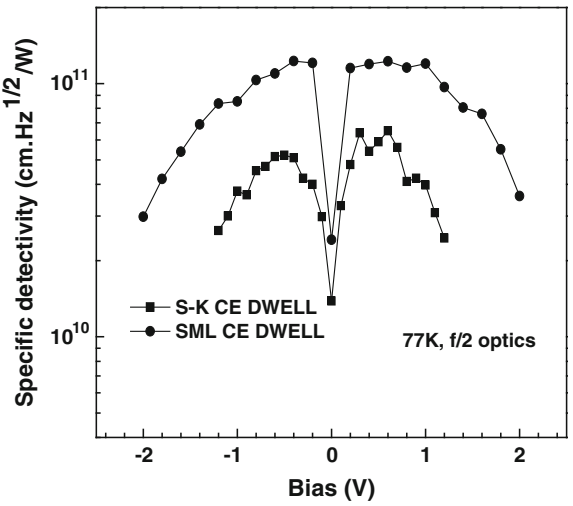

Fig. 4.15 Detectivity as a function of the applied bias voltage for S–K and SML QDIPs at 77 K. Reprinted from S. Sengupta et al., "Sub-monolayer quantum dots in confinement enhanced dots-in-a-well heterostructure", Applied Physics Letters, Vol. 100, p. 191111, 2012 with permission from AIP publishing LLC

$$G_{\mathrm{ph}} = i_{\mathrm{n}}^2 / \left(4e\Delta f \cdot I_{\mathrm{ph}}\right)$$

where i_{n}, e, Δf and I_{ph} are noise current, electronic charge, noise bandwidth and photocurrent, respectively. Figure 4.17 shows the results of PC gain and absorption quantum efficiency at 77 K. The PC gain proved to be lower than unity in the operating bias region.

The probable existence of excited states in a QW increases the capture probability, which justifies its low PC gain. The absorption efficiency reaches 7.0% at the operating bias and increases to 11.5% with an increase in bias. This high absorption QE is attributed to a strong overlap of electronic wave-function inside the dots. The

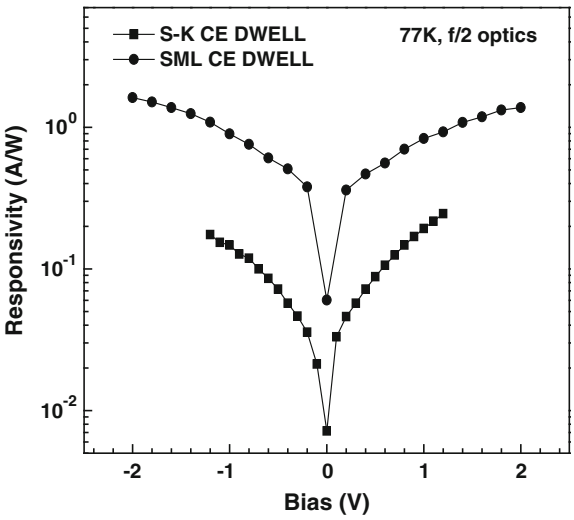

Fig. 4.16 Responsivity as a function of applied bias voltage of S–K and SML QDIPS at 77 K. Reprinted from S. Sengupta et al., "Sub-monolayer quantum dots in confinement enhanced dots-in-a-well heterostructure", Applied Physics Letters, Vol. 100, p. 191111, 2012 with permission from AIP publishing LLC

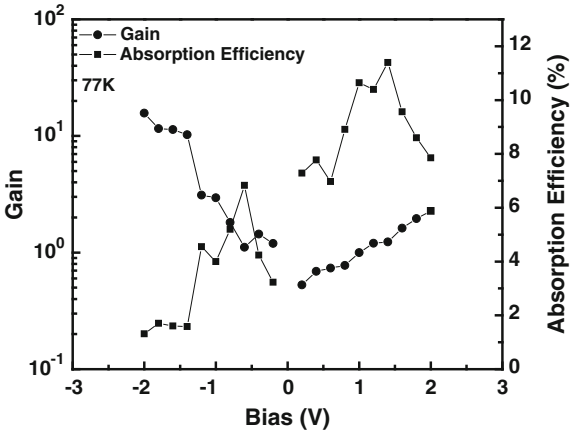

Fig. 4.17 Gain and absorption efficiency as a function of the applied bias voltage at 77 K for S–K and SML QDIPs. Reprinted from S. Sengupta et al., "Sub-monolayer quantum dots in confinement enhanced dots-in-a-well heterostructure", Applied Physics Letters, Vol. 100, p. 191111, 2012 with permission from AIP publishing LLC

presence of AlGaAs layer and the smaller dot size produces the improvement in wave-function coupling, which enhances the absorption strength of GS electrons. Figure 4.17 shows considerable enhancement in absorption QE for a SML CE DWELL compared to its S–K counterpart. It obtains high values of detectivity,

PC gain and absorption QE even at zero bias, resulting from a limitation of the measurement set-up during noise measurements. Those results are ignored.

4.4 Conclusions

We presented a comprehensive study of InAs sub-monolayer QDs with different capping combination layers such as GaAs, InGaAs-GaAs and InAlGaAs-GaAs for samples A, B and C, respectively, after performing an optimization study on InAs deposition thickness in single stack and thickness of capping layer. PL experiments at room temperature confirmed the existence of a GS-emission peak from the dots at 898, 917 and 867 nm for samples A, B and C, respectively. The FWHM was in the range of 19–32 meV, which indicates high uniformity of dot-size distribution. We calculated thermal-activation energies in the temperature-dependent PL experiment for samples A, B and C to be 49, 112 and 109 meV, respectively. We fabricated single-pixel photodetectors fabricated from samples A, B and C. Dark current was measured in the range of 10^{-5} to 10^{-4} A/cm^2 at a 0.5 V applied bias at 77 K.

We continued to explore the SML heterostructure using a different architecture, implementing the concept of a CE barrier with a DWELL architecture originally proposed for S–K QDIP devices. We studied the effect of varying the number of stacks inside the heterostructure. After a detailed investigation of optical and spectral properties, the 4-stack device sample emerged as the best device. We compared this SML device with a traditional S–K QD in CE DWELL architecture. The device characterization ensures high performance at a low operating bias at 77 K. The detectivity of the SML-based device was 1.2×10^{11} cm Hz$^{1/2}$ W^{-1} with a responsivity reaching 0.5 A/W (77 K, 0.4 V, 7.5 μm, *f*/2 optics). The typical operating bias for a SML QD detector is less than 1 V making them suitable for focal plane array (FPA) applications, where a low operating bias is essential due to the use of commercially available silicon read-out circuits.

References

1. L. Fu, P. Lever, K. Sears, H. Tan, C. Jagadish, In0: 5 Ga0: 5 As/GaAs quantum dot infrared photodetectors grown by metal-organic chemical vapor deposition. IEEE Electron Device Lett. **26** (2005)
2. S.D. Gunapala, S.V. Bandara, C.J. Hill, D.Z. Ting, J.K. Liu, S.B. Rafol et al., 640 × 512 pixels long-wavelength infrared (LWIR) quantum-dot infrared photodetector (QDIP) imaging focal plane array. IEEE J. Quantum Electron. **43**, 230–237 (2007)
3. L. Höglund, C. Asplund, Q. Wang, S. Almqvist, H. Malm, E. Petrini et al., Origin of photocurrent in lateral quantum dots-in-a-well infrared photodetectors. Appl. Phys. Lett. **88**, 213510 (2006)
4. S. Krishna, Quantum dots-in-a-well infrared photodetectors. Infrared Phys. Technol. **47**, 153–163 (2005)

5. Y.D. Sharma, M. Kutty, R. Shenoi, A.V. Barve, S. Myers, J. Shao et al., Investigation of multistack InAs/InGaAs/GaAs self-assembled quantum dots-in-double-well structures for infrared detectors. J. Vac. Sci. Technol. B **28,** C3G1-C3G7 (2010)
6. A. Barve, S. Shah, J. Shao, T. Vandervelde, R. Shenoi, W.-Y. Jang et al., Reduction in dark current using resonant tunneling barriers in quantum dots-in-a-well long wavelength infrared photodetector. Appl. Phys. Lett. **93**, 131115 (2008)
7. A. Barve, J. Shao, Y.D. Sharma, T.E. Vandervelde, K. Sankalp, S.J. Lee et al., Resonant tunneling barriers in quantum dots-in-a-well infrared photodetectors. IEEE J. Quantum Electron. **46**, 1105–1114 (2010)
8. S. Chakrabarti, A. Stiff-Roberts, P. Bhattacharya, S. Kennerly, High responsivity AlAs/InAs/GaAs superlattice quantum dot infrared photodetector. Electron. Lett. **40**, 197–198 (2004)
9. S. Chakrabarti, S. Adhikary, N. Halder, Y. Aytac, A. Perera, High-performance, long-wave ($\sim$10.2 μm) InGaAs/GaAs quantum dot infrared photodetector with quaternary In 0.21 Al 0.21 Ga 0.58 As capping. Appl. Phys. Lett. **99**, 181102–181102-3 (2011)
10. J. Vaillancourt, P. Vasinajindakaw, X. Lu, A high operating temperature (HOT) middle wave infrared (MWIR) quantum-dot photodetector. Opt. Photonics Lett. **4**, 57–61 (2011)
11. S. Chakrabarti, S. Adhikary, N. Halder, Y. Aytac, A. Perera, Demonstration of high responsivity ($\sim$2.16 A/W) and detectivity ($\sim$10 11 Jones) in the long wavelength ($\sim$10.2 μm) from InGaAs/GaAs quantum dot infrared photodetector with quaternary InAlGaAs capping. SPIE Def. Secur. Sens. 835338–835338-6 (2012)
12. M. Zavvari, V. Ahmadi, A. Mir, E. Darabi, Quantum dot infrared photodetector enhanced by avalanche multiplication. Electron. Lett. **48**, 589–591 (2012)
13. G. Ariyawansa, A.U. Perera, G. Raghavan, G. Von Winckel, A. Stintz, S. Krishna, Effect of well width on three-color quantum dots-in-a-well infrared detectors. IEEE Photonics Technol. Lett. **17**, 1064–1066 (2005)
14. A.V. Barve, J. Montaya, Y. Sharma, T. Rotter, J. Shao, W.-Y. Jang et al., High temperature operation of quantum dots-in-a-well infrared ssss. Infrared Phys. Technol. **54**, 215–219 (2011)
15. A. Barve, S. Sengupta, J. Kim, Y. Sharma, S. Adhikary, T. Rotter et al., Confinement enhancing barriers for high performance quantum dots-in-a-well infrared detectors. Appl. Phys. Lett. **99**, 191110 (2011)
16. V. Bressler-Hill, A. Lorke, S. Varma, P. Petroff, K. Pond, W. Weinberg, Initial stages of InAs epitaxy on vicinal GaAs (001)-(2 $\times$ 4). Phys. Rev. B **50**, 8479 (1994)
17. N. Ledentsov, P. Wang, C.S. Torres, A.Y. Egorov, M. Maximov, V. Ustinov et al., Optical spectroscopic studies of InAs layer transformation on GaAs surfaces. Phys. Rev. B **50**, 12171 (1994)
18. N. Ledentsov, A. Tsatsul'nikov, A.Y. Egorov, P. Kop'ev, A. Kovsh, M. Maximov, et al., Intrinsic optical confinement and lasing in InAs–AlGaAs submonolayer superlattices. Appl. phys. Lett. **74**, 161–163 (1999)
19. Z. Xu, J. Wang, Y. Wang, W.-K. Ge, Q. Li, S. Li et al., Wavelength tuning in GaAs/AlGaAs quantum wells by InAs submonolayer insertion. J. Phys. Condens. Matter **11**, 3629 (1999)
20. F.-I. Lai, H. Yang, G. Lin, I.-C. Hsu, J.-N. Liu, N. Maleev et al., High-power single-mode submonolayer quantum-dot photonic crystal vertical-cavity surface-emitting lasers. IEEE J. Sel. Top. Quantum Electron. **13**, 1318–1323 (2007)
21. A. Lenz, H. Eisele, J. Becker, L. Ivanova, E. Lenz, F. Luckert et al., Atomic structure of buried InAs sub-monolayer depositions in GaAs. Appl. Phys. Express **3**, 105602 (2010)
22. S. Krishna, D. Zhu, J. Xu, K. Linder, O. Qasaimeh, P. Bhattacharya et al., Structural and luminescence characteristics of cycled submonolayer InAs/GaAs quantum dots with room-temperature emission at 1.3 μm. J. Appl. Phys. **86**, 6135–6138 (1999)
23. Z. Xu, D. Birkedal, J.M. Hvam, Z. Zhao, Y. Liu, K. Yang et al., Structure and optical anisotropy of vertically correlated submonolayer InAs/GaAs quantum dots. Appl. Phys. Lett. **82**, 3859–3861 (2003)

24. N. Ledentsov, D. Bimberg, F. Hopfer, A. Mutig, V. Shchukin, A. Savel'ev et al., Submonolayer quantum dots for high speed surface emitting lasers. Nanoscale Res. Lett. **2**, 417–429 (2007)
25. A.R. Kovsh, A.E. Zhukov, N.A. Maleev, S.S. Mikhrin, D. Livshits, Y.M. Shernyakov et al., High power lasers based on submonolayer InAs–GaAs quantum dots and InGaAs quantum wells. Microelectron. J. **34**, 491–493 (2003)
26. Z. Xu, D. Birkedal, M. Juhl, J.M. Hvam, Submonolayer InGaAs/GaAs quantum-dot lasers with high modal gain and zero-linewidth enhancement factor. Appl. Phys. Lett. **85**, 3259 (2004)
27. L. Xin-Kun, J. Peng, L. De-Chun, W. Ju, W. Zhan-Guo, InAs/GaAs submonolayer quantum-dot superluminescent diodes with active multimode interferometer configuration. Chin. Phys. B **22**, 048102 (2013)
28. D.Z.-Y. Ting, S.V. Bandara, S.D. Gunapala, J.M. Mumolo, S.A. Keo, C.J. Hill et al., Submonolayer quantum dot sss. Appl. Phys. Lett. **94**, 111107 (2009)
29. S. Sengupta, A. Mandal, H. Ghadi, S. Chakrabarti, K.L. Mathur, Comprehensive study on molecular beam epitaxy-grown InAs sub-monolayer quantum dots with different capping combinations. J. Vac. Sci. Technol. B **31**, 03C136 (2013)
30. J. Kim, S. Sengupta, A. Barve, Y. Sharma, S. Adhikary, S. Lee et al., Multi-stack InAs/InGaAs sub-monolayer quantum dots sssss. Appl. Phys. Lett. **102**, 011131 (2013)
31. S. Sengupta, J.O. Kim, A.V. Barve, S. Adhikary, Y.D. Sharma, N. Gautam et al., Sub-monolayer quantum dots in confinement enhanced dots-in-a-well heterostructure. Appl. Phys. Lett. **100**, 191111–191111-4 (2012)

Index

B
Bilayer quantum dots, 26, 29, 31, 36, 41

C
Confinement enhancing barrier, 44

G
Growth pause, 14, 16–18, 20, 21

I
Infrared photodetector, 8, 10

M
Molecular beam aepitaxy, 4

P
Photodetectors, 2–4, 8, 21, 45, 48, 56
Photoluminescence, 7

Q
Quantum dots, 4, 16

R
Rapid thermal annealing, 9, 14, 19

S
Scanning electron microscope, 45
Sub-monolayer quantum dots, 44, 45, 56

T
Transmission electron microscope, 30

© Springer Nature Singapore Pte Ltd. 2018

S. Sengupta and S. Chakrabarti, *Structural, Optical and Spectral Behaviour of InAs-based Quantum Dot Heterostructures*,
DOI 10.1007/978-981-10-5702-1